Title

Microcalorimetry electrothermal impedance spectroscopy (ETIS) informs entropy evolution at individual electrodes of PNb_9O_{25} or $TiNb_2O_7$ battery cells

Authors

Zhou, Yucheng
Luo, Yunkai
Patterson, Ashlea
et al.

Publication Date

2023-11-01

DOI

10.1016/j.electacta.2023.143072

Peer reviewed

Microcalorimetry electrothermal impedance spectroscopy (ETIS) informs entropy evolution at individual electrodes of PNb_9O_{25} or $TiNb_2O_7$ battery cells

Yucheng Zhou[a], Yunkai Luo[b], Ashlea Patterson[c,d], Sun Woong Baek[a], Matevž Frajnkovič[a], Ram Seshadri[c,d], Bruce S. Dunn[b,e], and Laurent Pilon[a,e,f,+]

[a]Mechanical and Aerospace Engineering Department, Henry Samueli School of Engineering and Applied Science, University of California, Los Angeles, CA 90095, USA

[b]Materials Science and Engineering Department, Henry Samueli School of Engineering and Applied Science, University of California, Los Angeles, CA 90095, USA

[c]Materials Department, and Materials Research Laboratory, University of California, Santa Barbara, CA 93106, USA

[d]Department of Chemistry and Biochemistry, University of California, Santa Barbara, CA 93106, USA

[e]California NanoSystems Institute, University of California, Los Angeles, CA 90095, USA

[f]Institute of the Environment and Sustainability, University of California, Los Angeles, CA 90095, USA

[+]Corresponding Author: Phone: +1 (310)-206-5598, Fax: +1 (310)-206-2302

E-mail: pilon@seas.ucla.edu

August 9, 2023

Abstract

This study proposes a novel and fast microcalorimetry electrothermal impedance spectroscopy (ETIS) method based on heat generation rate measurements at each electrode of a lithium-ion battery cell. This new method is capable of retrieving the open-circuit voltage, the entropic potential, and the partial entropy changes at each electrode from measurements at a single temperature. It also shortens the measurement duration to a few hours compared to several days using the galvanostatic intermittent titration technique (GITT). The method consists of imposing a sinusoidal current on the cell assembled in an *operando* isothermal calorimeter. The induced sinusoidal potential response is used to calculate the open-circuit voltage of the cell as a function of the state of charge. The measured heat generation rates are analyzed by fast Fourier transform to determine not only the entropic potential of the cell but also the partial entropy changes at each electrode. This novel microcalorimetry ETIS method was first validated with numerical simulations. Then, it was experimentally demonstrated on battery cells consisting of PNb_9O_{25} or $TiNb_2O_7$ working electrodes and metallic lithium counter electrodes in 1 M $LiPF_6$ in EC:DMC 1:1 v/v electrolyte. The results of the open-circuit voltage and the normalized entropic potential matched those previously determined by potentiometric entropy measurements based on GITT measurements at different temperatures. Furthermore, while the normalized partial entropy changes exhibited notable features at the PNb_9O_{25} or $TiNb_2O_7$ working electrodes, they varied little at the metallic lithium counter electrodes.

Keywords: lithium-ion battery, open-circuit voltage, entropic potential, electrothermal impedance spectroscopy, calorimetry

1 Introduction

The global transition towards renewable energy and the widespread electrification of everything has led to significant interest in electrical energy storage systems including lithium-ion batteries (LIBs) [1–6]. Over the past decades, efforts have focused on discovering new cathode and anode materials with large capacity and long cycle life, among other attributes. Simultaneously, electrochemical methods of analysis have been developed to gain insight into their charging and discharging mechanisms.

The entropic potential $\partial U_{OCV}/\partial T$ of a battery cell is defined as the derivative of the cell open-circuit voltage U_{OCV} with respect to temperature T as a function of the state of charge. Both U_{OCV} and $\partial U_{OCV}/\partial T$ relate to thermodynamic properties whose measurement can provide insight into the charging mechanisms of LIBs and the reversible heat generation rate during cycling [7]. Multiple approaches have been proposed to measure the entropic potential of LIBs [8–16]. It can be determined by performing galvanostatic intermittent titration technique (GITT) at different temperatures. However, such measurements are time-consuming and usually require hundreds of hours for a single lithiation/delithiation cycle. Alternatively, the electrothermal impedance spectroscopy (ETIS) technique - first proposed by Schmidt et al. [17] and subsequently advanced by Hu et al. [18,19] - is capable of measuring the entropic potential of LIBs within only a few hours for one lithiation/delithiation cycle. However, these techniques use measurement apparatus that require substantial temperature changes and/or heat generation to produce accurate results. Therefore, so far they have been demonstrated only with commercial cylindrical and pouch cells with mass loadings on the order of grams. However, in laboratory settings it is more practical to synthesize electrodes with mass loadings on the order of milligrams of LIB materials [20–22]. Moreover, previous studies primarily focused on the entropic potential of the entire battery cell. However, the partial entropy changes at each electrode is also of interest, as they can uncover the thermodynamics behavior of the anode and cathode materials separately.

This study presents a novel microcalorimetry ETIS measurement method to rapidly determine the open-circuit voltage U_{OCV}, the entropic potential $\partial U_{OCV}/\partial T$, and the partial

entropy changes at each electrode of a battery cell. This new method uses an *operando* isothermal calorimeter capable of measuring the instantaneous heat generation rates at individual electrodes with small mass loadings. After validating the method using numerical simulations, it was demonstrated experimentally with PNb_9O_{25} or $TiNb_2O_7$ battery cells assembled in the calorimeter.

2 Background

2.1 Potentiometric entropy measurements

Potentiometric entropy measurements consist of determining the open-circuit voltage $U_{OCV}(x,T)$ and the entropic potential $[\partial U_{OCV}/\partial T](x,T)$ of a battery cell at a given temperature T and pressure as functions of lithium composition x, specific capacity C_m, or state of charge. Our previous study [7] has not only described the fundamental relationships between $U_{OCV}(x,T)$, $[\partial U_{OCV}/\partial T](x,T)$, and the material thermodynamic properties, but also developed an interpretation guide of their measurements for LIBs. In brief, the open-circuit voltage $U_{OCV}(x,T)$ of a battery cell with an intercalation compound (denoted by MA) working electrode and a metallic lithium (denoted by Li) counter electrode can be expressed as [7, 23],

$$U_{OCV}(x,T) = -\frac{1}{e}\left[\frac{\partial g_{MA}}{\partial x}(x,T) - \frac{\partial g_{Li}}{\partial x}(x,T)\right] \tag{1}$$

where e is the elementary charge, $g_{MA}(x,T)$ is the Gibbs free energy of Li_xMA per unit of MA, and $g_{Li}(x,T)$ is the Gibbs free energy per unit of metallic lithium. Similarly, the entropic potential $[\partial U_{OCV}/\partial T](x,T)$ can be expressed as [7, 24],

$$\frac{\partial U_{OCV}}{\partial T}(x,T) = \frac{1}{e}\left[\frac{\partial s_{MA}}{\partial x}(x,T) - \frac{\partial s_{Li}}{\partial x}(x,T)\right] \tag{2}$$

where $s_{MA}(x,T)$ is the entropy of Li_xMA per unit of MA and $s_{Li}(x,T)$ is the entropy per unit of metallic lithium. As such, $[\partial s_{MA}/\partial x](x,T)$ and $-[\partial s_{Li}/\partial x](x,T)$ can be regarded as the respective partial entropy changes at each electrode. Furthermore, the counter electrode

consists of macroscopic metallic lithium with negligible surface energy effects [25]. Thus, $[\partial g_{Li}/\partial x](x,T)$ corresponds to the standard Gibbs free energy per unit of metallic lithium $g^{\circ}_{Li}(T)$, and $-[\partial s_{Li}/\partial x](x,T)$ is equal to the standard entropy per unit of metallic lithium $-s^{\circ}_{Li}(T)$ [7, 26]. Both $g^{\circ}_{Li}(T)$ and $-s^{\circ}_{Li}(T)$ are independent of x. Finally, the evolution of $U_{OCV}(x,T)$ and $[\partial U_{OCV}/\partial T](x,T)$ during lithiation can provide insight into the charging mechanisms of the battery cell such as lithium ion insertion in a homogeneous solid solution, two-phase coexistence, phase transition, and intralayer lithium ion ordering [7].

Potentiometric entropy measurements consist of imposing a series of constant current pulses on the battery cell at constant temperature similar to GITT [27–29]. However, each current pulse is followed by a relaxation period during which a step-like temperature profile with four temperature plateaus is applied to the battery cell. Simultaneously, the corresponding potential evolution of the battery cell is recorded by a high accuracy potentiostat. As such, the open-circuit voltage $U_{OCV}(x,T)$ can be retrieved from the measured potential at the end of the relaxation period. Furthermore, the entropic potential $[\partial U_{OCV}/\partial T](x,T)$ can be calculated by taking the finite difference of the potential in response to each temperature step and averaging over the four instances. This method has been demonstrated to accurately measure the open-circuit voltage $U_{OCV}(x,T)$ and the entropic potential $[\partial U_{OCV}/\partial T](x,T)$ of coin cells with metallic lithium counter electrodes and working electrodes made of intercalation compounds such as graphite [7], $LiCoO_2$ [7], $LiFePO_4$ [7], $TiNb_2O_7$ [27], PNb_9O_{25} [28], $Ti_2Nb_2O_9$ [29], $LiScMo_3O_8$ [22], and Mo_4O_{11} [21]. However, it requires long relaxation periods to ensure that the battery cell has reached thermodynamic equilibrium before collecting data for each lithium composition x at each temperature T. In fact, the total measurement time for one lithiation/delithiation cycle of a coin cell usually ranges between 200 and 400 hours [27–29]. Such durations are prohibitively long and faster alternative methods capable of providing meaningful information would be highly desirable.

2.2 *Operando* isothermal calorimetry

Heat generation arises from multiple physicochemical phenomena occurring inside electrochemical energy storage systems during operation [30]. Therefore, accurate estimations of heat generation are essential in designing effective thermal management strategies to prevent potential fire hazards such as thermal runaway [31]. Accordingly, various calorimetric techniques have been developed to measure the heat generation in batteries including accelerating rate calorimetry [31, 32], differential scanning calorimetry [33, 34], and isothermal calorimetry [30]. In particular, several isothermal calorimetric studies have reported heat generation rates in coin cells [30, 34], cylindrical cells [35], Swagelok cells [33], and prismatic cells [31] under galvanostatic cycling. However, they only detected the heat generation rate for the entire cell. To overcome this limitation, Munteshari et al. [36] developed and validated experimentally an *operando* isothermal calorimeter capable of measuring the instantaneous heat generation rates at each electrode. Subsequently, the device has been used to measure heat generation rates at each electrode of electric double layer capacitors [36–41], hybrid pseudocapacitors [42, 43], and LIBs [27–29]. The measurements revealed the thermal signatures associated with physical, chemical, and transport processes including resistive losses [27–29, 38–43], entropic changes [28, 29], ion adsorption/desorption [38–43], ion solvation/desolvation [28, 43], enthalpy of mixing [27, 28], electrolyte decomposition [40, 41, 43], overscreening effect [37, 41], and insulator to metal transition [27, 28].

2.3 Fast Fourier transform (FFT)

Fast Fourier transform (FFT) is an algorithm computing the discrete Fourier transform of a sequence and converting it from time domain to frequency domain [44]. It is an effective tool to reveal any periodically oscillating feature within a signal which may not be obvious from its temporal evolution. For example, let us consider a signal which can be represented by the function $f(t)$ over time t such that,

$$f(t) = A_0 + A_A \cos(2\pi f_A t + \phi_A) + A_B \cos(2\pi f_B t + \phi_B) + \cdots \tag{3}$$

By applying FFT to $f(t)$, the amplitudes (A_A, A_B, $\cdots$), frequencies (f_A, f_B, $\cdots$), and phase angles (ϕ_A, ϕ_B, $\cdots$) of every sinusoidal term can be identified. Note that the phase angle given by FFT has a range between -π and π.

2.4 Electrothermal impedance spectroscopy (ETIS)

Previously, multiple characterization techniques have been developed to enable the simultaneous analysis of both electrochemical and thermal behavior of electrical energy storage systems. For example, Hess et al. [45] designed an in situ simultaneous thermal analysis (STA) cell for electric double layer capacitors. This technique monitors the change in heat flow, mass loss, resistance, and capacitance within electric double layer capacitors during operation. It was employed to investigate the impact of operating voltage and temperature on the cycling degradation of electric double-layer capacitors and on the associated thermal processes occurring within the devices [45–47]. Similarly for LIBs, Schmidt et al. [17] first proposed ETIS as an alternative to the time-consuming potentiometric entropy measurements based on GITT. The ETIS method consists of imposing on a battery cell a current $I(t)$ with a very small constant offset I_0 and a sinusoidal oscillation with amplitude I_1 at frequency f_1, i.e.,

$$I(t) = I_0 + I_1 \sin(2\pi f_1 t). \tag{4}$$

Note that I_0 is small enough to be negligible compared to I_1, i.e., $|I_0| \ll |I_1|$. Under such conditions, the irreversible Joule heating $\dot{Q}_J(t)$ can be expressed as [17],

$$\dot{Q}_J(t) = I(t)^2 R \approx -\frac{{I_1}^2 R}{2}\cos(4\pi f_1 t) + \frac{{I_1}^2 R}{2} \tag{5}$$

where R is the internal resistance of the battery cell. Similarly, the reversible entropic heat generation rate $\dot{Q}_{rev}(t)$ can be written as [17],

$$\dot{Q}_{rev}(t) = I(t) T_m \frac{\partial U_{OCV}}{\partial T}(x,T) \approx I_1 T_m \frac{\partial U_{OCV}}{\partial T}(x,T)\sin(2\pi f_1 t) \tag{6}$$

where T_m is the measured cell temperature averaged over the sinusoidal period.

The measured instantaneous temperature response $T_{cell}(t)$ of the battery cell can be expressed as [17],

$$T_{cell}(t) = T_{amb} + \Delta T_J(t) + \Delta T_{rev}(t) \tag{7}$$

where T_{amb} is the ambient temperature (assumed to be constant) while $\Delta T_J(t)$ and $\Delta T_{rev}(t)$ are the cell temperature changes due to irreversible Joule heating and reversible entropic heat generation, respectively. The thermal impedance $Z_{th}(f)$ (in K/W) of a battery cell at frequency f can be defined as,

$$Z_{th}(f) = \frac{T_{cell}(f) - T_{amb}(f)}{\dot{Q}_T(f)} = \frac{\Delta T_J(f) + \Delta T_{rev}(f)}{\dot{Q}_J(f) + \dot{Q}_{rev}(f)}. \tag{8}$$

Note that in the frequency domain, $T_{amb}(f) = 0$ unless $f = 0$. As such, the cell temperature changes $\Delta T_J(t)$ and $\Delta T_{rev}(t)$ were related to the heat generation rates $\dot{Q}_J(t)$ and $\dot{Q}_{rev}(t)$ through the thermal impedance $Z_{th}(f)$ of the battery cell such that [17],

$$\Delta T_J(t) = -\frac{{I_1}^2 R}{2} \left|Z_{th}(2f_1)\right| \cos\left[4\pi f_1 t + \phi_{Z_{th}}(2f_1)\right] + \frac{{I_1}^2 R}{2} \left|Z_{th}(2f_1)\right|, \text{ and} \tag{9}$$

$$\Delta T_{rev}(t) = I_1 T_m \frac{\partial U_{OCV}}{\partial T}(x,T) \left|Z_{th}(f_1)\right| \sin\left[2\pi f_1 t + \phi_{Z_{th}}(f_1)\right] \tag{10}$$

where the thermal impedance $Z_{th}(f)$ can be defined as a frequency-dependent complex function with magnitude $|Z_{th}(f)|$ and phase difference $\phi_{Z_{th}}(f)$ at frequency f. Here, the sinusoidal oscillations within $\Delta T_J(t)$ and $\Delta T_{rev}(t)$ have distinct frequencies $2f_1$ and f_1, respectively. Thus, they can be distinguished in the frequency domain by applying FFT to the measured $T_{cell}(t)$. In fact, Schmidt et al. [17] expressed the amplitude $A_T(2f_1)$ associated with the temperature oscillation at frequency $2f_1$ as,

$$A_T(2f_1) = \frac{{I_1}^2 R}{2} \left|Z_{th}(2f_1)\right| \tag{11}$$

and $A_T(f_1)$ at frequency f_1 as,

$$A_T(f_1) = I_1 T_m \frac{\partial U_{OCV}}{\partial T}(x,T) \left|Z_{th}(f_1)\right|. \tag{12}$$

As a result, the internal resistance R can be retrieved from the FFT output $A_T(2f_1)$ as,

$$R = \frac{2}{{I_1}^2 \left|Z_{th}(2f_1)\right|} A_T(2f_1). \tag{13}$$

Similarly, the entropic potential $[\partial U_{OCV}/\partial T](x,T)$ can be obtained from the FFT output $A_T(f_1)$ as,

$$\frac{\partial U_{OCV}}{\partial T}(x,T) = \frac{1}{I_1 T_m \left|Z_{th}(f_1)\right|} A_T(f_1). \tag{14}$$

To obtain the thermal impedance magnitudes $|Z_{th}(2f_1)|$ and $|Z_{th}(f_1)|$, the following procedure was suggested [17]. First, the entropic potential of the battery cell at a given state of charge (SOC) is predetermined by potentiometric entropy measurements based on GITT at four different temperatures. Then, the battery cell is set to this SOC and excited with a sinusoidal current at frequency $2f_1$. As the entropic potential at this SOC is known, the reversible entropic heat generation rate $\dot{Q}_{rev}(t)$ can be calculated using Equation (6). Simultaneously, the instantaneous temperature response $T_{cell}(t)$ of the battery cell is measured. Subsequently, both the measured $T_{cell}(t)$ and the calculated $\dot{Q}_{rev}(t)$ are analyzed by FFT. This identifies the amplitudes of the sinusoidal oscillations at frequency $2f_1$ within $T_{cell}(t)$ and $\dot{Q}_{rev}(t)$. Finally, the thermal impedance magnitude $|Z_{th}(2f_1)|$ arises as the ratio of these two amplitudes, i.e., $|Z_{th}(2f_1)| = |T_{cell}(2f_1)| \,/\, \left|\dot{Q}_{rev}(2f_1)\right|$. The same procedure is repeated at frequency f_1 to obtain the thermal impedance magnitude $|Z_{th}(f_1)|$, i.e., $|Z_{th}(f_1)| = |T_{cell}(f_1)| \,/\, \left|\dot{Q}_{rev}(f_1)\right|$.

Overall, this method was successfully demonstrated on commercial cylindrical and pouch cells with capacities around 1 Ah [17]. The retrieved entropic potential $[\partial U_{OCV}/\partial T](x,T)$ agreed with that determined by potentiometric entropy measurements based on GITT, and the measurement duration was shortened from several days to a few hours [17]. Nevertheless, in practice this method becomes unnecessarily complicated because of the requirement to measure the temperature. First, accurate values of the thermal impedance magnitudes $|Z_{th}(2f_1)|$ and $|Z_{th}(f_1)|$ must be obtained. The thermal impedance serves as the only available relationship from the measured temperature response $T_{cell}(t)$ back to the heat generation rates $\dot{Q}_J(t)$ and $\dot{Q}_{rev}(t)$ in the battery cell which are not directly measured. However, several studies have illustrated that the thermal impedance can vary substantially with minor changes in ambient temperature [48] and ambient relative humidity [49]. Thus, consistent conditions must be maintained for the duration of the experiment. For example, throughout their experiment, Schmidt et al. [17] placed the battery cell and mounted the temperature

sensor in the same positions. Furthermore, the entire setup was housed in an incubator to ensure constant ambient temperature and ambient relative humidity. Moreover, the imposed sinusoidal current needs to have large amplitude (on the order of amperes) and low frequency (on the order of millihertz) to create temperature oscillations on the order of a few degrees Celsius which are detectable by conventional temperature sensors [17]. These criteria are challenging for battery cells with large thermal conductivity and/or large specific heat capacity, as a larger heat generation rate is required to induce sufficiently large temperature oscillations [48].

To address these drawbacks, Hu et al. [18, 19] attempted to eliminate the step of retrieving the heat generation rate from the measured temperature response. Instead, they directly measured the total heat generation rate $\dot{Q}_T(t)$ using an isothermal calorimeter at temperature T_m [18, 19]. The imposed current $I(t)$ was given by Equation (4) and $\dot{Q}_T(t)$ was expressed as the sum of $\dot{Q}_J(t)$ and $\dot{Q}_{rev}(t)$ given by Equations (5) and (6), respectively. Therefore, after applying FFT to the measured $\dot{Q}_T(t)$, they expressed the amplitude $A_Q(2f_1)$ associated with the heat generation rate oscillation at frequency $2f_1$ as,

$$A_Q(2f_1) = \frac{{I_1}^2 R}{2} \tag{15}$$

and $A_Q(f_1)$ at frequency f_1 as,

$$A_Q(f_1) = I_1 T_m \frac{\partial U_{OCV}}{\partial T}(x, T). \tag{16}$$

Then, the internal resistance R and the entropic potential $[\partial U_{OCV}/\partial T](x, T)$ can be retrieved from the FFT output $A_Q(2f_1)$ and $A_Q(f_1)$ as,

$$R = \frac{2}{{I_1}^2} A_Q(2f_1) \tag{17}$$

$$\frac{\partial U_{OCV}}{\partial T}(x, T) = \frac{1}{I_1 T_m} A_Q(f_1). \tag{18}$$

This modified ETIS method was successfully demonstrated on a commercial LMO-NMC/graphite pouch cell with a capacity of 25.9 Ah [18, 19]. The isothermal calorimeter measured the heat generation rate and retrieved the entropic potential of the entire pouch

cell. It simplified the experimental procedure and improved the accuracy of the retrieved entropic potential and internal resistance [18,19]. However, the isothermal calorimeter had a maximum measurement error of 0.67 W and a response time of at least a few seconds [18,19]. Thus, its most appropriate application is for commercial pouch cells with mass loadings on the order of grams. However, in the discovery of novel LIB materials in a laboratory setting, one typically synthesizes electrodes with mass loadings on the order of a few mg/cm^2 tested in coin cells with heat generation rates on the order of microwatts [27–29]. For coin cells, an isothermal calorimeter with considerably better sensitivity and shorter response time is necessary to capture the instantaneous heat generation rate typically featuring rapid fluctuations of relatively small magnitudes [36]. In addition, measuring the heat generation rates at each electrode could be used to investigate their individual partial entropy changes. This could provide insight into the thermodynamics behavior of both the anode and the cathode and contribute in selecting the pair of electrodes for full cells.

This study aims to develop a novel microcalorimetry ETIS measurement method to quickly determine the open-circuit voltage U_{OCV} and the entropic potential $\partial U_{OCV}/\partial T$ of battery cells with electrode mass loadings on the order of milligrams and fabricated in a laboratory setting. This new method uses an *operando* isothermal calorimeter designed to measure the instantaneous heat generation rates on the order of microwatts at individual electrodes, making it the first method capable of investigating the partial entropy changes at each electrode during cycling.

3 Analysis

3.1 Imposed current

Figure 1 shows the schematic of the new procedure developed to determine the open-circuit voltage $U_{OCV}(x,T)$ and the entropic potential $[\partial U_{OCV}/\partial T](x,T)$ of an LIB cell from microcalorimetry ETIS measurements. The apparatus consists of the *operando* isothermal calorimeter described in Ref. [36] and reproduced in Figure 2 for the sake of completeness.

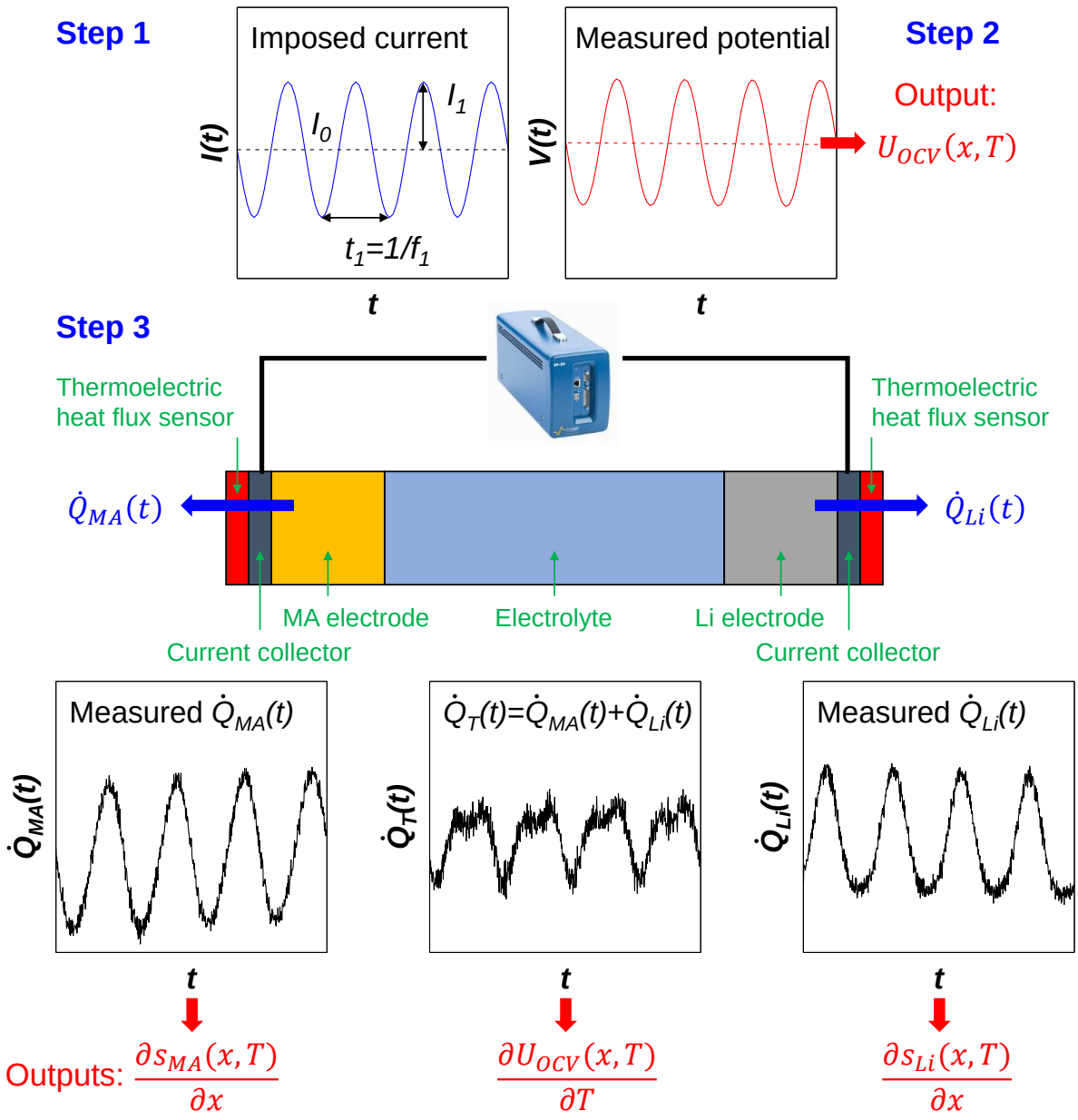

Figure 1: Schematic of the procedure and experimental apparatus developed to determine the open-circuit voltage $U_{OCV}(x,T)$ and the entropic potential $[\partial U_{OCV}/\partial T](x,T)$ of an LIB cell from the novel microcalorimetry ETIS measurements.

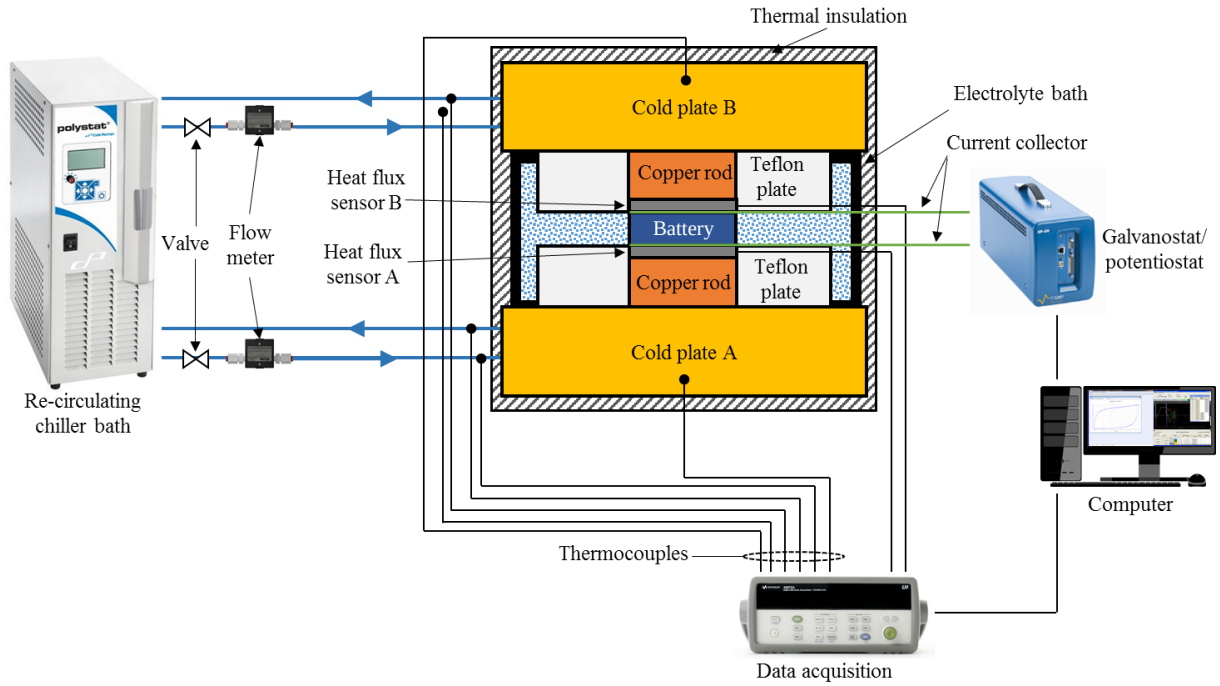

Figure 2: Schematic of the *operando* isothermal calorimeter used in microcalorimetry ETIS measurements.

Battery cells consisting of two bare electrodes cast on current collectors and two thick separators impregnated with electrolyte are assembled in the calorimeter and cycled using a high accuracy potentiostat. Instantaneous heat generation rates at individual electrodes are measured by thermoelectric heat flux sensors in thermal contact with the back of each electrode.

To complement previous studies [17–19], here we describe how to retrieve the open-circuit voltage from the measured cell potential and the entropic potential as well as the partial entropy changes at each electrode from the measured instantaneous heat generation rates. The technique starts by imposing a current $I(t)$ consisting of a constant offset I_0 and a sinusoidal function oscillating with amplitude I_1 at frequency f_1, i.e.,

$$I(t) = I_0 - I_1 \sin(2\pi f_1 t) = I_0 + I_1 \cos\left(2\pi f_1 t + \frac{\pi}{2}\right). \tag{19}$$

As discussed in detail by Schmidt et al. [17], the choice of I_0, I_1, and f_1 is a compromise among several different considerations. Here, I_0 is negative which slowly but continuously discharges the battery cell. Note also that I_0 should be negligible compared to I_1, i.e., $|I_0| \ll |I_1|$. However, a large magnitude of I_0 results in faster discharging and thus quicker measurements. Similarly, I_1 should be large enough to ensure an adequate signal-to-noise ratio in the measured oscillating heat generation rates. However, a small I_1 is preferable as (i) it maximizes the proportion of reversible entropic heat generation $\dot{Q}_{rev}(t)$ compared to Joule heating $\dot{Q}_J(t)$ and (ii) it minimizes the sinusoidal variation in the lithium composition x over a period. In fact, every data point of the open-circuit voltage $U_{OCV}(x,T)$ and the entropic potential $[\partial U_{OCV}/\partial T](x,T)$ retrieved by microcalorimetry ETIS measurements is actually the time-average over a sinusoidal period of an oscillating variable function of x. Therefore, this uncertainty can be alleviated by reducing the variation in x, which in turn improves the resolution of the retrieved $U_{OCV}(x,T)$ and $[\partial U_{OCV}/\partial T](x,T)$. In addition, f_1 should be sufficiently large to acquire enough data points. Here also, a large frequency f_1 shortens the period of every sinusoid, reduces the variation in x, and improves the resolution of the retrieved results. However, every period needs to last at least a few seconds to provide sufficient time for the periodically alternating redox reactions to occur within the battery

cell. Finally, the phase angle of $I(t)$ is chosen as $\pi/2$ such that (i) $I(t) \approx 0$ at $t = 0$ to avoid a sudden load on the potentiostat at the start of the measurements and (ii) $I(t)$ is negative during the first half-period to avoid overcharging the battery cell when it already begins in fully charged (delithiated) state.

The elapsed time t (in s) can be converted into the lithium composition x in $\mathrm{Li}_x\mathrm{MA}$ such that,

$$x(t) = -\frac{x_{theo}\Delta q(t)}{3600 m C_{m,theo}} = -\frac{x_{theo}\int_0^t I(t')\mathrm{d}t'}{3600 m C_{m,theo}}. \tag{20}$$

Here, $\Delta q(t)$ (in mC) is the amount of charge transferred to the battery cell between times 0 and t, $I(t)$ (in mA) is the imposed current given by Equation (19), m (in g) is the mass loading of active material MA, and $C_{m,theo}$ (in mAh/g) is the theoretical specific capacity of the intercalation compound corresponding to the theoretical lithium composition x_{theo}. For example, in the case of a PNb_9O_{25} working electrode, $C_{m,theo} = 190$ mAh/g assuming $x_{theo} = 9$ [28], while for a $TiNb_2O_7$ working electrode, $C_{m,theo} = 388$ mAh/g assuming $x_{theo} = 5$ [27].

3.2 Potential response and open-circuit voltage

Under the imposed current $I(t)$ of Equation (19) and assuming $|I_0| \ll |I_1|$, the measured potential response $V(t)$ can be expressed as,

$$V(t) = U_{OCV}(x,T) + I_1\,|Z(f_1)|\cos\left[2\pi f_1 t + \frac{\pi}{2} + \phi_Z(f_1)\right]. \tag{21}$$

Here, $Z(f_1)$ (in Ω) is the electrochemical impedance of the battery cell at frequency f_1. Note that $Z(f_1)$ is a complex number such that $Z(f_1) = Z_{re}(f_1) + iZ_{im}(f_1)$. Alternatively, $Z(f_1)$ can be described by its magnitude $|Z(f_1)|$ and phase difference $\phi_Z(f_1)$, i.e., $Z(f_1) = |Z(f_1)|\exp[i\phi_Z(f_1)]$ [50, 51]. Accordingly, the open-circuit voltage $U_{OCV}(x_i,T)$ at lithium composition x_i can be calculated by averaging the measured cell potential $V(t)$ over a period such that,

$$U_{OCV}(x_i,T) = \frac{1}{t_1}\int_{(i-1)t_1}^{it_1} V(t')\mathrm{d}t' \tag{22}$$

where $t_1 = 1/f_1$ is the period of $I(t)$ and time t falls within this period from $(i-1)t_1$ to it_1. In other words, $U_{OCV}(x,T)$ is considered equal to $U_{OCV}(x_i,T)$ for any lithium composition x between x_{i-1} and x_i such that,

$$x_i = -\frac{x_{theo}\int_0^{it_1} I(t')\mathrm{d}t'}{3600mC_{m,theo}}. \tag{23}$$

3.3 Heat generation rates

The total instantaneous heat generation rate $\dot{Q}_T(t)$ in a battery cell can be divided into several contributions including (i) Joule heating $\dot{Q}_J(t)$, (ii) reversible entropic heat generation $\dot{Q}_{rev}(t)$, (iii) enthalpy of mixing $\dot{Q}_{mix}(t)$, and (iv) heat generation due to side reactions $\dot{Q}_{sr}(t)$, i.e. [27–30, 52, 53],

$$\dot{Q}_T(t) = \dot{Q}_J(t) + \dot{Q}_{rev}(t) + \dot{Q}_{mix}(t) + \dot{Q}_{sr}(t). \tag{24}$$

The heat generation rate $\dot{Q}_J(t)$ associated with irreversible resistive losses can be expressed as [27–30, 52, 53],

$$\dot{Q}_J(t) = I(t)\left[V(t) - U_{OCV}(x,T)\right]. \tag{25}$$

Substituting $I(t)$ given by Equation (19) (assuming $|I_0| \ll |I_1|$) and $V(t)$ given by Equation (21) into Equation (25) yields,

$$\dot{Q}_J(t) = \frac{{I_1}^2}{2}|Z(f_1)|\cos\left[4\pi f_1 t + \pi + \phi_Z(f_1)\right] + \frac{{I_1}^2}{2}|Z(f_1)|\cos\left[\phi_Z(f_1)\right]. \tag{26}$$

Similarly, the reversible heat generation rate $\dot{Q}_{rev}(t)$ due to entropic changes can be expressed as [30, 52, 53],

$$\dot{Q}_{rev}(t) = I(t)T\frac{\partial U_{OCV}}{\partial T}(x,T). \tag{27}$$

Here, T is the temperature of the battery cell imposed to be constant during *operando* isothermal calorimetry. Although $[\partial U_{OCV}/\partial T](x,T)$ is a real number, for the convenience of FFT analysis we describe it by its magnitude $|[\partial U_{OCV}/\partial T](x,T)|$ and phase difference ϕ_{rev}. Then, substituting $I(t)$ given by Equation (19) into Equation (27) and assuming $|I_0| \ll |I_1|$ yields,

$$\dot{Q}_{rev}(t) = I_1 T\left|\frac{\partial U_{OCV}}{\partial T}(x,T)\right|\cos\left(2\pi f_1 t + \frac{\pi}{2} + \phi_{rev}\right). \tag{28}$$

Mathematically during discharging (lithiation) with negative $I(t)$, if $\phi_{rev} \approx 0$ then $[\partial U_{OCV}/\partial T](x,T)$ is positive and $\dot{Q}_{rev}(t)$ is endothermic, or if $\phi_{rev} \approx \pi$ then $[\partial U_{OCV}/\partial T](x,T)$ is negative and $\dot{Q}_{rev}(t)$ is exothermic.

Furthermore, $\dot{Q}_{rev}(t)$ can be defined as the sum of the reversible heat generation rates at the intercalation compound working electrode $\dot{Q}_{rev,MA}(t)$ and at the metallic lithium counter electrode $\dot{Q}_{rev,Li}(t)$ such that $\dot{Q}_{rev}(t) = \dot{Q}_{rev,MA}(t) + \dot{Q}_{rev,Li}(t)$ [28,29]. Then, $\dot{Q}_{rev,MA}(t)$ can be expressed as,

$$\dot{Q}_{rev,MA}(t) = \frac{I(t)T}{e}\frac{\partial s_{MA}}{\partial x}(x,T) = \frac{I_1 T}{e}\left|\frac{\partial s_{MA}}{\partial x}(x,T)\right|\cos\left(2\pi f_1 t + \frac{\pi}{2} + \phi_{rev,MA}\right). \quad (29)$$

Here also, the partial entropy change at the intercalation compound working electrode $[\partial s_{MA}/\partial x](x,T)$ is a real number that can be described by its magnitude $|[\partial s_{MA}/\partial x](x,T)|$ and its phase difference $\phi_{rev,MA}$. Similarly, $\dot{Q}_{rev,Li}(t)$ can be written as,

$$\dot{Q}_{rev,Li}(t) = -\frac{I(t)T}{e}\frac{\partial s_{Li}}{\partial x}(x,T) = \frac{I_1 T}{e}\left|\frac{\partial s_{Li}}{\partial x}(x,T)\right|\cos\left(2\pi f_1 t + \frac{3\pi}{2} + \phi_{rev,Li}\right). \quad (30)$$

Finally, $\dot{Q}_{mix}(t)$ is the heat generation rate associated with the enthalpy of mixing caused by ion concentration gradients. Here, $\dot{Q}_{mix}(t)$ is related to the local values of the partial molar enthalpy and the concentration gradient of each ion species in the battery cell [30, 52, 53]. These parameters are difficult to know for any given location within the cell at any given time. Therefore, an exact relationship between $\dot{Q}_{mix}(t)$ and $I(t)$ cannot be established. Nevertheless, $\dot{Q}_{mix}(t)$ is typically negligible at low C-rates [52], as assumed in the present FFT analysis. Furthermore, the heat generation rate due to side reactions $\dot{Q}_{sr}(t)$ is generally neglected unless the battery cell is operating under extreme conditions [30, 52–54].

3.4 Entropic potential and partial entropy changes

Substituting Equations (26) and (28) into Equation (24) yields,

$$\dot{Q}_T(t) = A_{tot}(0) + A_{tot}(f_1)\cos\left[2\pi f_1 t + \phi_{tot}(f_1)\right] + A_{tot}(2f_1)\cos\left[4\pi f_1 t + \phi_{tot}(2f_1)\right] \quad (31)$$

where the terms $A_{tot}(0)$, $A_{tot}(f_1)$, and $A_{tot}(2f_1)$ are given by,

$$A_{tot}(0) = \frac{{I_1}^2}{2} |Z(f_1)| \cos\left[\phi_Z(f_1)\right], \tag{32}$$

$$A_{tot}(f_1) = I_1 T \left| \frac{\partial U_{OCV}}{\partial T}(x,T) \right|, \text{ and} \tag{33}$$

$$A_{tot}(2f_1) = \frac{{I_1}^2}{2} |Z(f_1)|. \tag{34}$$

Applying FFT to the measured $\dot{Q}_T(t)$ during a given period from $(i-1)t_1$ to it_1 yields the amplitude $A_{tot}(f_1)$ of the sinusoidal oscillation at frequency f_1 given by Equation (33) and the corresponding phase angle $\phi_{tot}(f_1)$ expressed as,

$$\phi_{tot}(f_1) = \frac{\pi}{2} + \phi_{rev}. \tag{35}$$

Thus, the entropic potential $[\partial U_{OCV}/\partial T](x_i, T)$ at discrete lithium composition x_i can be written as,

$$\frac{\partial U_{OCV}}{\partial T}(x_i,T) = \left| \frac{\partial U_{OCV}}{\partial T}(x,T) \right| \cos\left(\phi_{rev}\right) = \frac{A_{tot}(f_1)}{I_1 T} \cos\left[\phi_{tot}(f_1) - \frac{\pi}{2}\right]. \tag{36}$$

Similarly, FFT can also be applied to the instantaneous heat generation rates $\dot{Q}_{MA}(t)$ measured at the intercalation compound working electrode and $\dot{Q}_{Li}(t)$ measured at the metallic lithium counter electrode, both during the same period from $(i-1)t_1$ to it_1. Applying FFT to $\dot{Q}_{MA}(t)$ given by Equation (29) yields the amplitude $A_{MA}(f_1)$ of the sinusoidal oscillation at frequency f_1 expressed as,

$$A_{MA}(f_1) = \frac{I_1 T}{e} \left| \frac{\partial s_{MA}}{\partial x}(x,T) \right| \tag{37}$$

while the phase angle $\phi_{MA}(f_1)$ is given by,

$$\phi_{MA}(f_1) = \frac{\pi}{2} + \phi_{rev,MA}. \tag{38}$$

Then, the partial entropy change at the intercalation compound working electrode $[\partial s_{MA}/\partial x](x_i, T)$ at discrete lithium composition x_i can be written as,

$$\frac{\partial s_{MA}}{\partial x}(x_i,T) = \frac{A_{MA}(f_1) e}{I_1 T} \cos\left[\phi_{MA}(f_1) - \frac{\pi}{2}\right]. \tag{39}$$

Likewise, applying FFT to $\dot{Q}_{Li}(t)$ given by Equation (30) yields the amplitude $A_{Li}(f_1)$ of the sinusoidal oscillation at frequency f_1 expressed as,

$$A_{Li}(f_1) = \frac{I_1 T}{e} \left| \frac{\partial s_{Li}}{\partial x}(x, T) \right| \tag{40}$$

while the phase angle $\phi_{Li}(f_1)$ is given by,

$$\phi_{Li}(f_1) = \frac{3\pi}{2} + \phi_{rev,Li}. \tag{41}$$

Thus, the partial entropy change at the metallic lithium counter electrode $-[\partial s_{Li}/\partial x](x_i, T)$ at discrete lithium composition x_i can be written as,

$$-\frac{\partial s_{Li}}{\partial x}(x_i, T) = -s^{\circ}_{Li}(T) = \frac{A_{Li}(f_1)e}{I_1 T} \cos\left[\phi_{Li}(f_1) - \frac{\pi}{2}\right]. \tag{42}$$

4 Materials and methods

4.1 Synthesis of PNb_9O_{25} powder

To synthesize the PNb_9O_{25} powder, 0.9 mmol of Nb_2O_5 (Sigma Aldrich, 99.99%) and 0.2 mmol of $NH_4H_2PO_4$ (Sigma Aldrich, 98%) powders were mixed. This mixture was ground with a pestle in an agate mortar for 10 minutes to obtain a homogeneous powder. This powder was transferred into an alumina crucible and placed in a tube furnace with Ar flow at room temperature for 2 hours to get rid of air. The furnace was first heated to 350 °C at 1 °C/minute of ramp rate where it was maintained for 8 hours with Ar flow. Then, the Ar flow was stopped and the furnace was heated to 1000 °C at 5 °C/minute of ramp rate where it was maintained for 24 hours. Finally, this sample was naturally cooled down to room temperature to obtain PNb_9O_{25} powder.

4.2 Synthesis of $TiNb_2O_7$ powder

To synthesize the $TiNb_2O_7$ powder, TiO_2 (Sigma Aldrich, 99%) and Nb_2O_5 (Materion, 99.95%) powders were mixed in stoichiometric ratio. This mixture was ground with a pestle

in an agate mortar for 30 minutes to obtain a homogeneous powder. Then, 300 mg of this powder was pressed into a pellet. The latter was placed on a bed of sacrificial powder of the same material in an alumina crucible, which was nestled into a larger alumina crucible filled with 7 g of activated charcoal. This stack was heated in a microwave oven at 1125 W for 8 to 9 minutes. Finally, the insulation was removed and the $TiNb_2O_7$ pellet was left to cool to room temperature.

4.3 Electrode fabrication

To fabricate the PNb_9O_{25} or $TiNb_2O_7$ electrodes, the previously synthesized PNb_9O_{25} powder or $TiNb_2O_7$ pellet was mixed with SuperP (TIMCAL) and ground with a pestle in an agate mortar for 10 minutes. To prepare the PNb_9O_{25} or $TiNb_2O_7$ slurry, polyvinylidene fluoride (PVDF) was first dissolved in N-Methyl-2-pyrrolidone (NMP). The PNb_9O_{25}/SuperP or $TiNb_2O_7$/SuperP mixture was then added to the PVDF/NMP solution. The resulting slurry had a PNb_9O_{25} or $TiNb_2O_7$:SuperP:PVDF mass ratio of 7.5:1.5:1. Finally, the slurry was cast on a large copper foil using a doctor blade adjusted to the desired gap. The electrodes were first dried on a 40 °C hot plate overnight and then dried in a 110 °C vacuum oven for 6 hours. The thickness of the PNb_9O_{25} electrodes was around 40 μm and their PNb_9O_{25} mass loading was around 2 mg/cm^2. For the $TiNb_2O_7$ electrodes, the thickness was around 20 μm and the $TiNb_2O_7$ mass loading was around 1 mg/cm^2. Note that X-ray diffraction spectra, cyclic voltammetry, and galvanostatic cycling measurements of similar cells with PNb_9O_{25} or $TiNb_2O_7$ electrodes made using the same material synthesis and electrode fabrication methods can be found in our previous studies [27, 28].

4.4 *Operando* isothermal calorimeter

Microcalorimetry ETIS measurements were performed in an *operando* isothermal calorimeter described in Ref. [36]. Here, the two-electrode calorimetric battery cells consisted of (i) a PNb_9O_{25} or $TiNb_2O_7$ working electrode previously fabricated and cut into 1 cm × 1 cm square shape, (ii) a polished metallic lithium (Sigma Aldrich, 99.9%) counter electrode also

cut into 1 cm × 1 cm square shape, (iii) two 260 μm thick glass microfiber filters (Whatman, Grade GF/C) acting as both separators and thermal insulators, impregnated with (iv) 1 M $LiPF_6$ in EC:DMC 1:1 v/v (Sigma Aldrich, battery grade) electrolyte. Note that the two-electrode calorimetric battery cells were assembled in a glove box containing Ar gas with less than 0.1 ppm of O_2 and H_2O.

During microcalorimetry ETIS measurements, the current was imposed and the potential was measured using a high accuracy potentiostat (BioLogic, SP-150). Simultaneously, the instantaneous heat generation rates $\dot{Q}_i(t)$ (in mW) at the PNb_9O_{25} or $TiNb_2O_7$ working electrode and at the metallic lithium counter electrode were calculated from the instantaneous heat fluxes $q''_i(t)$ (in mW/cm^2) measured by a 1 cm × 1 cm thermoelectric heat flux sensor (greenTEG, gSKIN-XP) in thermal contact with the back of each electrode "i" according to [36],

$$\dot{Q}_i(t) = q''_i(t)A_i = \frac{\Delta V_i(t)}{S_i}A_i \quad \text{with } i = MA \text{ or } Li. \tag{43}$$

Here, A_i (in cm^2) is the footprint area of the electrode and $\Delta V_i(t)$ (in μV) is the instantaneous voltage difference measured by the heat flux sensor with sensitivity S_i [in μV/(W/cm^2)]. Then, the total instantaneous heat generation rate in the battery cell $\dot{Q}_T(t)$ can be expressed as the sum of those at each electrode, i.e.,

$$\dot{Q}_T(t) = \dot{Q}_{MA}(t) + \dot{Q}_{Li}(t). \tag{44}$$

5 Results and discussion

5.1 Numerical simulations of microcalorimetry ETIS

To evaluate the data analysis procedure previously described, numerical simulations of the novel microcalorimetry ETIS method were performed. The open-circuit voltage $U_{OCV}(x,T)$ and the entropic potential $[\partial U_{OCV}/\partial T](x,T)$ of a PNb_9O_{25} battery cell as functions of lithium composition x previously obtained experimentally from GITT measurements [28] were used as input parameters. In addition, the following parameters were imposed: (i) the ambient

temperature was T = 293.15 K, (ii) the electrochemical impedance of the battery cell was defined as $|Z(f_1)|$ = 100 Ω and $\phi_Z(f_1)$ = -π/6, and (iii) the data acquisition period was Δt = 0.1 s. The offset (I_0 = -0.05, -0.1, or -0.2 mA), amplitude (I_1 = 0.5, 1, or 2 mA), and frequency (f_1 = 25, 50, or 100 mHz) of the imposed current $I(t)$ calculated according to Equation (19) were realistic values typical of experimental measurements. Based on the imposed current $I(t)$, the corresponding lithium composition x at time t was calculated according to Equation (20). If x fell between any two nearest compositions x_1 and x_2 available from the GITT dataset, then the value of $U_{OCV}(x,T)$ was interpolated linearly between $U_{OCV}(x_1,T)$ and $U_{OCV}(x_2,T)$. Then, the potential response $V(t)$ was calculated according to Equation (21). Likewise, the value of $[\partial U_{OCV}/\partial T](x,T)$ was also interpolated between $[\partial U_{OCV}/\partial T](x_1,T)$ and $[\partial U_{OCV}/\partial T](x_2,T)$ given by GITT. Then, the irreversible $\dot{Q}_J(t)$ and reversible $\dot{Q}_{rev}(t)$ heat generation rates were calculated according to Equations (25) and (27), respectively. The sum gave the total instantaneous heat generation rate $\dot{Q}_T(t)$ such that $\dot{Q}_T(t) = \dot{Q}_J(t) + \dot{Q}_{rev}(t)$. Note that, in the present microcalorimetry ETIS method, the battery cell is assumed to be operating at low C-rates, such that the heat generation rates $\dot{Q}_{mix}(t)$ associated with the enthalpy of mixing and $\dot{Q}_{sr}(t)$ due to side reactions both become negligible. Moreover, to reproduce actual experimental measurements, white noise was added to the calculated $\dot{Q}_T(t)$ with signal-to-noise ratio equal to ∞, 10, or 5. By applying FFT to the calculated heat generation rate $\dot{Q}_T(t)$ with white noise, $[\partial U_{OCV}/\partial T](x,T)$ was determined according to Equation (36).

Figure 3 plots the entropic potential $[\partial U_{OCV}/\partial T](x,T)$ of a PNb_9O_{25} battery cell retrieved from numerical simulations of microcalorimetry ETIS after applying FFT to the calculated $\dot{Q}_T(t)$ with white noise for different values of (a) current offset I_0, (b) current amplitude I_1, (c) current frequency f_1, and (d) signal-to-noise ratio (SNR). The baseline case corresponds to T = 293.15 K, I_0 = -0.1 mA, I_1 = 1 mA, f_1 = 50 mHz, and SNR = ∞. Figure 3 also compares the retrieved entropic potential $[\partial U_{OCV}/\partial T](x,T)$ with the input parameters previously obtained experimentally with GITT at 20 °C [28]. Here, it is interesting to note that the choice of I_0 had a strong impact on the retrieved $[\partial U_{OCV}/\partial T](x,T)$ while the influ-

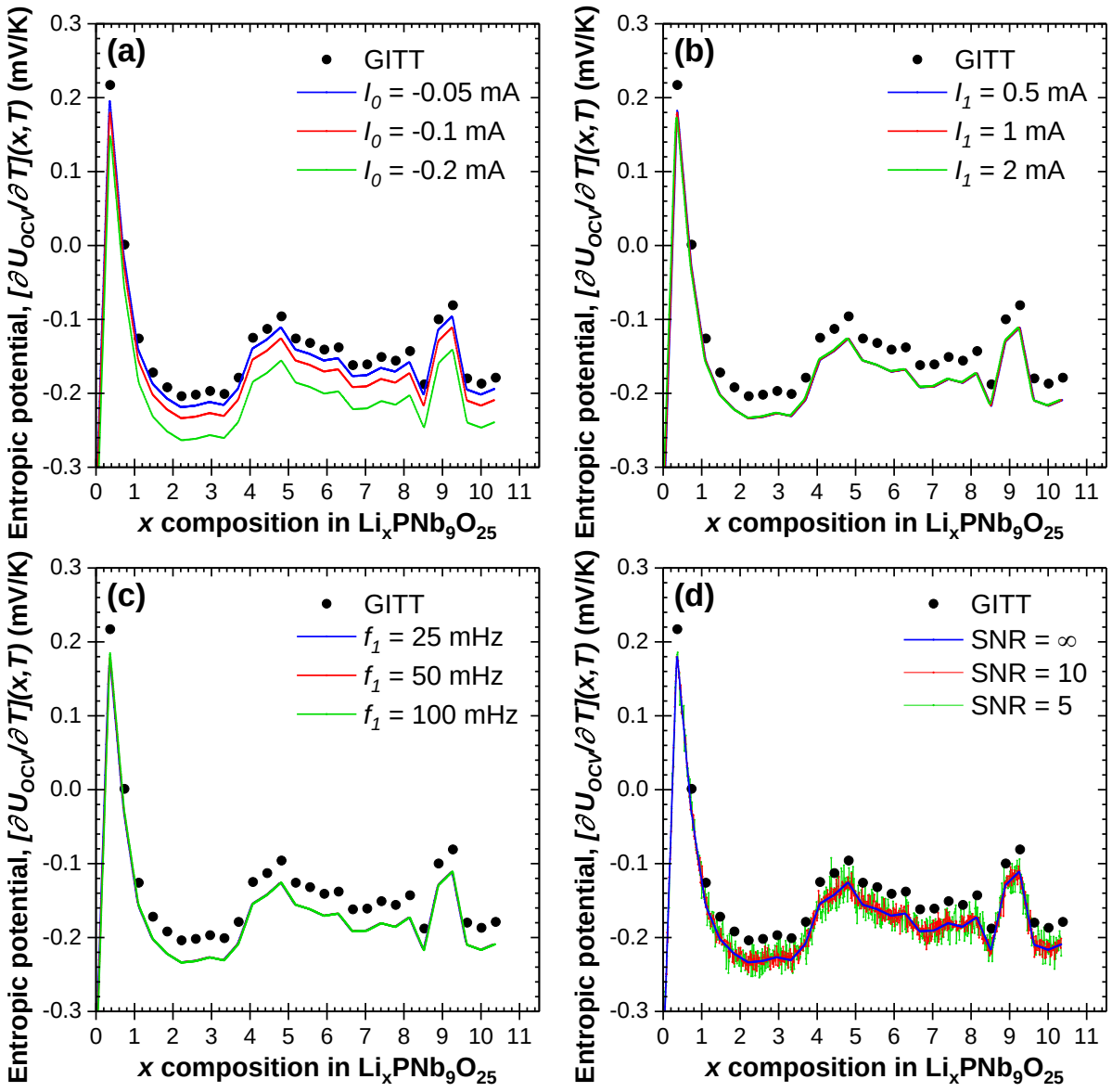

Figure 3: Entropic potential $[\partial U_{OCV}/\partial T](x,T)$ of a PNb_9O_{25} battery cell retrieved from numerical simulations of microcalorimetry ETIS for different values of (a) current offset I_0, (b) current amplitude I_1, (c) current frequency f_1, and (d) signal-to-noise ratio (SNR), with comparison to the $[\partial U_{OCV}/\partial T](x,T)$ obtained experimentally from GITT [28] and used as input. Unless otherwise noted, T = 293.15 K, I_0 = -0.1 mA, I_1 = 1 mA, f_1 = 50 mHz, and SNR = ∞.

ence of I_1 and f_1 was less visible. In fact, the deviation of the retrieved $[\partial U_{OCV}/\partial T](x,T)$ relative to that obtained from GITT was reduced by minimizing I_0. Nevertheless, in every case the $[\partial U_{OCV}/\partial T](x,T)$ retrieved from simulations accurately reflected the evolution of $[\partial U_{OCV}/\partial T](x,T)$ imposed and obtained experimentally from GITT. Finally, Figure 3(d) illustrates that even with a signal-to-noise ratio of 10 the evolution of $[\partial U_{OCV}/\partial T](x,T)$ can be successfully retrieved.

Furthermore, the profile of $[\partial U_{OCV}/\partial T](x,T)$ with respect to x is generally more informative than its magnitude. In fact, the former was sufficient in creating the interpretation guide of different charging mechanisms from our previous study [7]. Therefore, the retrieved entropic potential $[\partial U_{OCV}/\partial T](x,T)$ can be normalized according to,

$$\left[\frac{\partial U_{OCV}}{\partial T}\right]^{*}(x,T) = \frac{[\partial U_{OCV}/\partial T](x,T) - [\partial U_{OCV}/\partial T]_{min}(x,T)}{[\partial U_{OCV}/\partial T]_{max}(x,T) - [\partial U_{OCV}/\partial T]_{min}(x,T)} \tag{45}$$

where $[\partial U_{OCV}/\partial T]_{max}(x,T)$ and $[\partial U_{OCV}/\partial T]_{min}(x,T)$ are respectively the maximum and minimum values of the entropic potential over the entire window of lithium composition. Figure 4 plots the normalized entropic potential $[\partial U_{OCV}/\partial T]^{*}(x,T)$ for the same cases as those presented in Figure 3. First, in every case the relative difference between the normalized entropic potential $[\partial U_{OCV}/\partial T]^{*}(x,T)$ retrieved from simulations and that obtained experimentally from GITT (Figure 4) was smaller than the difference between their original values (Figure 3). This illustrates the fact that normalization can alleviate the impact of the arbitrary choice of I_0 while accurately retrieving the features of $[\partial U_{OCV}/\partial T]^{*}(x,T)$ necessary for its interpretation. In addition, the results can be further improved by minimizing I_1 and maximizing f_1. These observations can inform the experimental implementation of the present microcalorimetry ETIS method.

5.2 Microcalorimetry ETIS measurements on a battery cell

5.2.1 Imposed current and potential response

To validate experimentally the novel microcalorimetry ETIS method, measurements using *operando* isothermal calorimetry were performed on battery cells at temperature $T = 293.15$

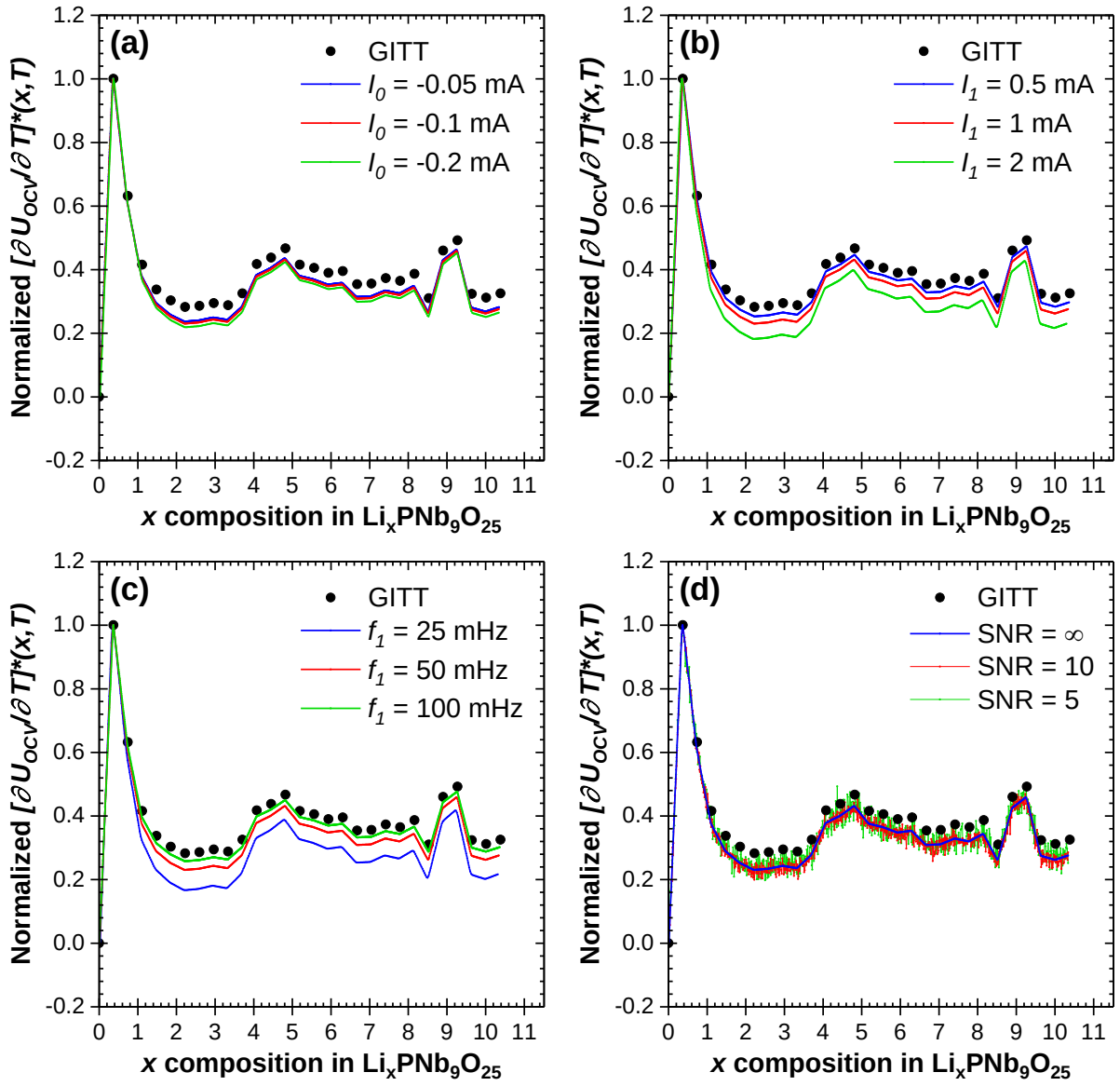

Figure 4: Normalized entropic potential $[\partial U_{OCV}/\partial T]^*(x,T)$ of the results shown in Figure 3 for a PNb_9O_{25} battery cell retrieved from numerical simulations of microcalorimetry ETIS for different values of (a) current offset I_0, (b) current amplitude I_1, (c) current frequency f_1, and (d) signal-to-noise ratio (SNR), with comparison to the normalized entropic potential $[\partial U_{OCV}/\partial T]^*(x,T)$ obtained experimentally from GITT [28] and used as input.

K. Here, the full cell was assembled in the *operando* isothermal calorimeter previously described with a PNb_9O_{25} or $TiNb_2O_7$ working electrode and a metallic lithium counter electrode immersed in 1 M $LiPF_6$ in EC:DMC 1:1 v/v electrolyte. The experimentally imposed current $I(t)$ during discharging (lithiation) featured offset I_0 = -0.1 mA, amplitude I_1 = 1 mA, frequency f_1 = 50 mHz, and period t_1 = 20 s. Note that these settings were chosen as a compromise between (i) superior accuracy of results calling for small I_0, small I_1, and large f_1, and (ii) the constraints of actual experimental conditions favoring large I_0 for shorter measurement duration, large I_1 for adequate heat generation rate signal, and small f_1 to give redox reactions sufficient time to proceed.

Figure 5 plots the measured potential $V(t)$ and the retrieved open-circuit voltage $U_{OCV}(x,T)$ determined using Equation (22) as the average of $V(t)$ over every period. As predicted by Equation (21), the sinusoidal oscillation of $V(t)$ was at the same frequency f_1 as $I(t)$. The overall duration for this discharging half-cycle was 5 hours for the PNb_9O_{25} battery cell and 3 hours for the $TiNb_2O_7$ battery cell, compared to 150 hours and 90 hours, respectively, for potentiometric entropy measurements based on GITT [28].

5.2.2 Heat generation rates

Figure 6 plots the instantaneous heat generation rates (a) $\dot{Q}_{PNO}(t)$ measured at the PNb_9O_{25} working electrode or (b) $\dot{Q}_{TNO}(t)$ measured at the $TiNb_2O_7$ working electrode, as well as $\dot{Q}_{Li}(t)$ measured at the corresponding metallic lithium counter electrode, and (c) $\dot{Q}_T(t) = \dot{Q}_{PNO}(t) + \dot{Q}_{Li}(t)$ or (d) $\dot{Q}_T(t) = \dot{Q}_{TNO}(t) + \dot{Q}_{Li}(t)$ measured in the entire battery cell over four consecutive periods. Interestingly, $\dot{Q}_{PNO}(t)$, $\dot{Q}_{TNO}(t)$, and $\dot{Q}_{Li}(t)$ were all sinusoidal functions with the same frequency f_1 as $I(t)$ and $V(t)$. As a result, $\dot{Q}_T(t)$ was periodic with complex patterns and period $t_1 = 1/f_1$ = 20 s. Moreover, $\dot{Q}_{PNO}(t)$ or $\dot{Q}_{TNO}(t)$ was endothermic (< 0) for negative current $I(t)$ and exothermic (> 0) for positive $I(t)$, whereas $\dot{Q}_{Li}(t)$ was exothermic for negative $I(t)$ and endothermic for positive $I(t)$. In fact, according to Equations (29) and (30), such behavior indicates that the partial entropy changes were positive at the PNb_9O_{25} or $TiNb_2O_7$ working electrodes and negative at the corresponding

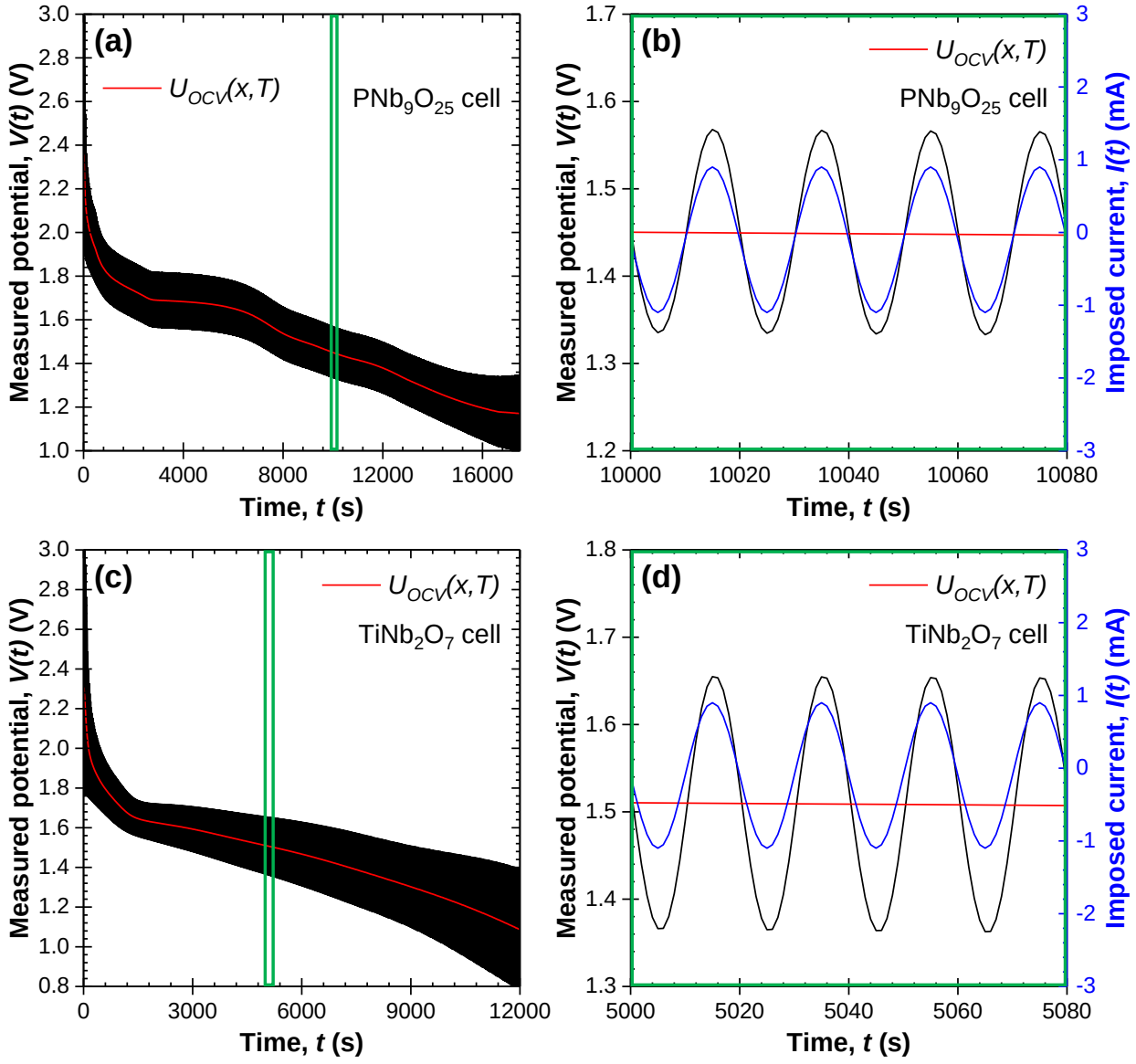

Figure 5: Measured potential $V(t)$ during discharging and retrieved open-circuit voltage $U_{OCV}(x,T)$ determined using Equation (22) as the average of $V(t)$ over every period during microcalorimetry ETIS measurements on a (a, b) PNb_9O_{25} or (c, d) $TiNb_2O_7$ battery cell. The imposed current $I(t)$ was given by Equation (19) with I_0 = -0.1 mA, I_1 = 1 mA, and f_1 = 50 mHz. Note that Figures 5(b) and 5(d) are enlargements of arbitrary time windows shown in green in Figures 5(a) and 5(c), respectively.

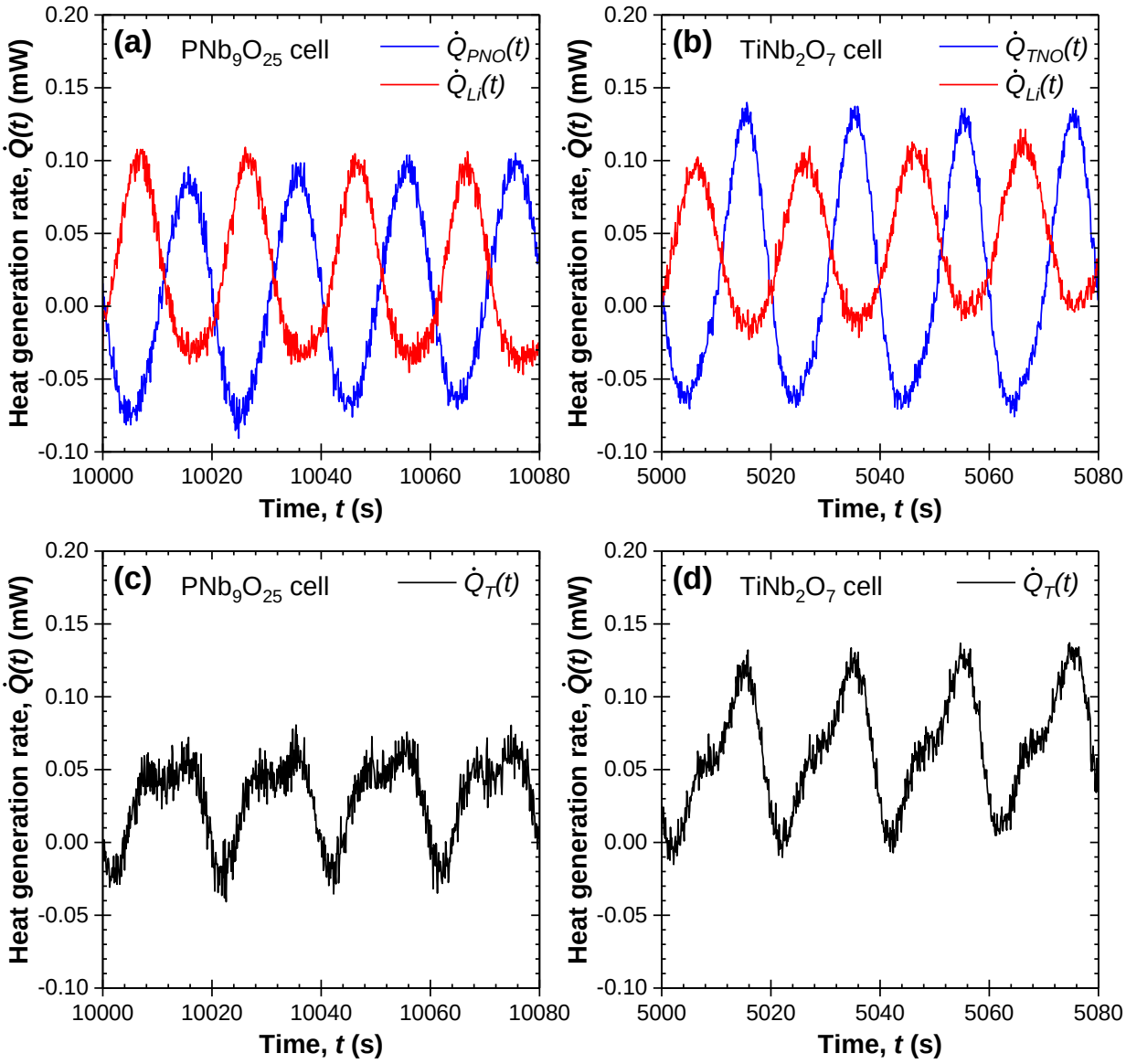

Figure 6: (a, b) Instantaneous heat generation rates (a) $\dot{Q}_{PNO}(t)$ measured at the PNb_9O_{25} working electrode or (b) $\dot{Q}_{TNO}(t)$ measured at the $TiNb_2O_7$ working electrode and $\dot{Q}_{Li}(t)$ measured at the corresponding metallic lithium counter electrode over four consecutive periods. (c, d) Total instantaneous heat generation rate (c) $\dot{Q}_T(t) = \dot{Q}_{PNO}(t) + \dot{Q}_{Li}(t)$ or (d) $\dot{Q}_T(t) = \dot{Q}_{TNO}(t) + \dot{Q}_{Li}(t)$ measured in the entire (c) PNb_9O_{25} or (d) $TiNb_2O_7$ battery cell.

metallic lithium counter electrodes. These results were consistent with the observations made in our previous study [28]. Finally, even though state-of-the-art potentiostat and heat flux sensors were used, Figure 6 illustrates that with $I_1 = 1$ mA and $f_1 = 50$ mHz, the signal-to-noise ratio in the measured heat generation rates was already around 10. Based on the numerical simulation results shown in Figure 3(d), a signal-to-noise ratio of at least 10 was necessary to successfully retrieve the evolution of $[\partial U_{OCV}/\partial T](x,T)$. Further decreasing I_1 and/or increasing f_1 would decrease the magnitude of the heat generation rates and, consequently, the signal-to-noise ratio would fall below 10 which would compromise the precision of the retrieved $[\partial U_{OCV}/\partial T](x,T)$.

5.2.3 Open-circuit voltage and entropic potential

After applying FFT to the total heat generation rate $\dot{Q}_T(t)$ in each battery cell, the entropic potential $[\partial U_{OCV}/\partial T](x,T)$ was determined according to Equation (36). The entropic potential was then normalized to compute $[\partial U_{OCV}/\partial T]^*(x,T)$ according to Equation (45). Figure 7 compares the open-circuit voltage $U_{OCV}(x,T)$ and the normalized entropic potential $[\partial U_{OCV}/\partial T]^*(x,T)$ of the investigated (a, b) PNb_9O_{25} or (c, d) $TiNb_2O_7$ battery cell determined by GITT [28] and by microcalorimetry ETIS measurements. Here, $U_{OCV}(x,T)$ and $[\partial U_{OCV}/\partial T]^*(x,T)$ determined by both methods were in very good agreement for both battery cells. In fact, while GITT only offered a limited number of data points, hundreds of data points were acquired from microcalorimetry ETIS which created continuous curves for $U_{OCV}(x,T)$ and $[\partial U_{OCV}/\partial T]^*(x,T)$. This is particularly noticeable for the PNb_9O_{25} cell for $0 < x < 0.5$ and for the $TiNb_2O_7$ cell for $3.2 < x < 4.3$, when sharp changes in $[\partial U_{OCV}/\partial T]^*(x,T)$ occurred but were not captured by the GITT method. In addition, combining the profiles of both $U_{OCV}(x,T)$ and $[\partial U_{OCV}/\partial T]^*(x,T)$ enables the identification of different regions with distinctive features [28].

For the PNb_9O_{25} battery cell, seven regions could be identified [7]. (i) Region I for $0 < x < 0.5$: U_{OCV} decreased sharply as a result of lithium intercalation in a homogeneous solid solution [28]. By contrast, $[\partial U_{OCV}/\partial T]^*$ featured a sharp peak and a maximum. This

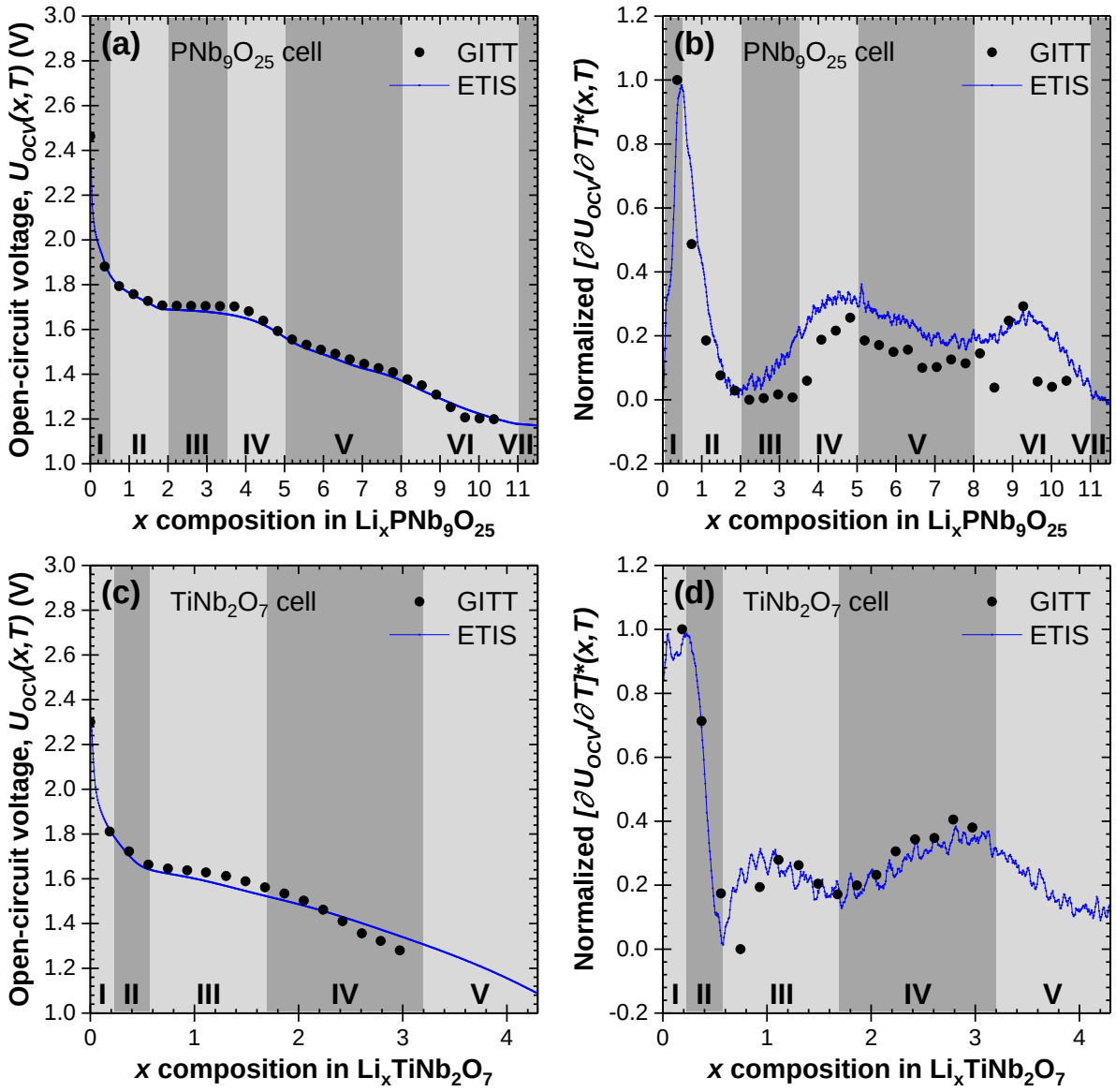

Figure 7: (a, c) Open-circuit voltage $U_{OCV}(x,T)$ and (b, d) normalized entropic potential $[\partial U_{OCV}/\partial T]^*(x,T)$ of a PNb_9O_{25} or $TiNb_2O_7$ battery cell determined by GITT [28] or microcalorimetry ETIS measurements. The different colored regions correspond to specific phenomena occurring in the battery cell.

can be attributed to the fact that PNb_9O_{25} is an insulator in pristine phase but quickly becomes a semiconductor upon lithiation [20, 55]. As the electrical conductivity increases, so does the electronic entropy, which in turn led to an increase in $[\partial U_{OCV}/\partial T]^*$ [28]. Note that this was not captured by previous GITT measurements. (ii) Region II for $0.5 < x < 2$: both U_{OCV} and $[\partial U_{OCV}/\partial T]^*$ decreased indicating lithium intercalation in a homogeneous solid solution and the associated configurational entropy change [7]. (iii) Region III for $2 < x < 3.5$: U_{OCV} plateaued as a sign of phase transition accompanied by two-phase coexistence [7]. Curiously, $[\partial U_{OCV}/\partial T]^*$ retrieved from microcalorimetry ETIS increased as opposed to staying relatively constant in GITT measurements. Note that PNb_9O_{25} has also been reported to undergo a semiconductor-to-metal transition around this range of lithium composition [20,55]. It is possible that microcalorimetry ETIS could not capture the plateau in $[\partial U_{OCV}/\partial T]^*$ associated with two-phase coexistence as effectively as GITT. In fact, phase transition is a kinetically slow process, which is captured by the long relaxation periods of GITT but not by microcalorimetry ETIS due to the constant switching between lithiation/delithiation half-periods arising from the sinusoidal current $I(t)$. (iv) Region IV for $3.5 < x < 5$: U_{OCV} decreased again suggesting lithium intercalation in a homogeneous solid solution [7]. Moreover, $[\partial U_{OCV}/\partial T]^*$ first increased then decreased resulting in a local maximum, during which the semiconductor-to-metal transition was completed [28]. (v) Region V for $5 < x < 8$: this region also featured lithium intercalation in a homogeneous solid solution as both U_{OCV} and $[\partial U_{OCV}/\partial T]^*$ decreased monotonously [7]. (vi) Region VI for $8 < x < 11$: the decrease in U_{OCV} was accompanied by a tilde-shaped fluctuation in $[\partial U_{OCV}/\partial T]^*$, which can be attributed to intralayer ion ordering [7]. It is interesting to note that the intralayer ion ordering spanned a wider range of lithium composition when measured by microcalorimetry ETIS than by GITT. Likewise, this difference possibly emerged as a result of the constant switching between lithiation/delithiation half-periods during microcalorimetry ETIS measurements, which might have prolonged the ion ordering process. (vii) Region VII for $11 < x < 11.5$: both U_{OCV} and $[\partial U_{OCV}/\partial T]^*$ featured a plateau indicative of phase transition accompanied by two-phase coexistence.

In the case of the $TiNb_2O_7$ battery cell, five regions could be identified [27]. (i) Region I for $0 < x < 0.2$: U_{OCV} featured a sharp drop indicating lithium intercalation in a homogeneous solid solution [7]. By contrast, $[\partial U_{OCV}/\partial T]^*$ rose to reach a maximum. This can also be attributed to the rapid electrical conductivity increase of $TiNb_2O_7$ upon lithiation [27,56]. (ii) Region II for $0.2 < x < 0.6$: both U_{OCV} and $[\partial U_{OCV}/\partial T]^*$ decreased due to lithium intercalation in a homogeneous solid solution [7]. The configurational entropy change contributed to the sharp decrease in $[\partial U_{OCV}/\partial T]^*$ [7]. (iii) Region III for $0.6 < x < 1.7$: U_{OCV} decreased slowly while $[\partial U_{OCV}/\partial T]^*$ featured a tilde-shaped fluctuation characteristic of intralayer ion ordering [7]. (iv) Region IV for $1.7 < x < 3.2$: U_{OCV} continued decreasing while $[\partial U_{OCV}/\partial T]^*$ first increased then decreased resulting in a local maximum. This behavior can be attributed to the continuous electrical conductivity increase of $TiNb_2O_7$ during lithiation [27,56]. Here also, the electronic entropy increased like the semiconductor-to-metal transition observed within region IV of the PNb_9O_{25} cell, thus leading to an analogous shape of the entropic potential. (v) Region V for $3.2 < x < 4.3$: both U_{OCV} and $[\partial U_{OCV}/\partial T]^*$ decreased monotonously corresponding to lithium intercalation in a homogeneous solid solution [7]. Note that this last region was observed only in the microcalorimetry ETIS method. In fact, our previous GITT measurements [27, 28] imposed a cell potential cutoff of 1 V to prevent the formation of solid electrolyte interphase (SEI) and dendrites in the battery cell under continuous discharging below 1 V [57, 58]. During microcalorimetry ETIS measurements though, the sinusoidal current $I(t)$ meant that whenever the cell potential went below 1 V, it only lasted a few seconds before the direction of current flow and ion diffusion was reversed again. This enabled the cell potential cutoff to be lower than 1 V without significantly damaging the battery cell. In particular, the potential of the $TiNb_2O_7$ cell was allowed to reach as low as 0.8 V during microcalorimetry ETIS measurements.

5.2.4 Partial entropy changes

FFT analysis was also applied to the heat generation rates $\dot{Q}_{PNO}(t)$ or $\dot{Q}_{TNO}(t)$ and $\dot{Q}_{Li}(t)$ measured at each electrode to determine the partial entropy changes at the PNb_9O_{25} or

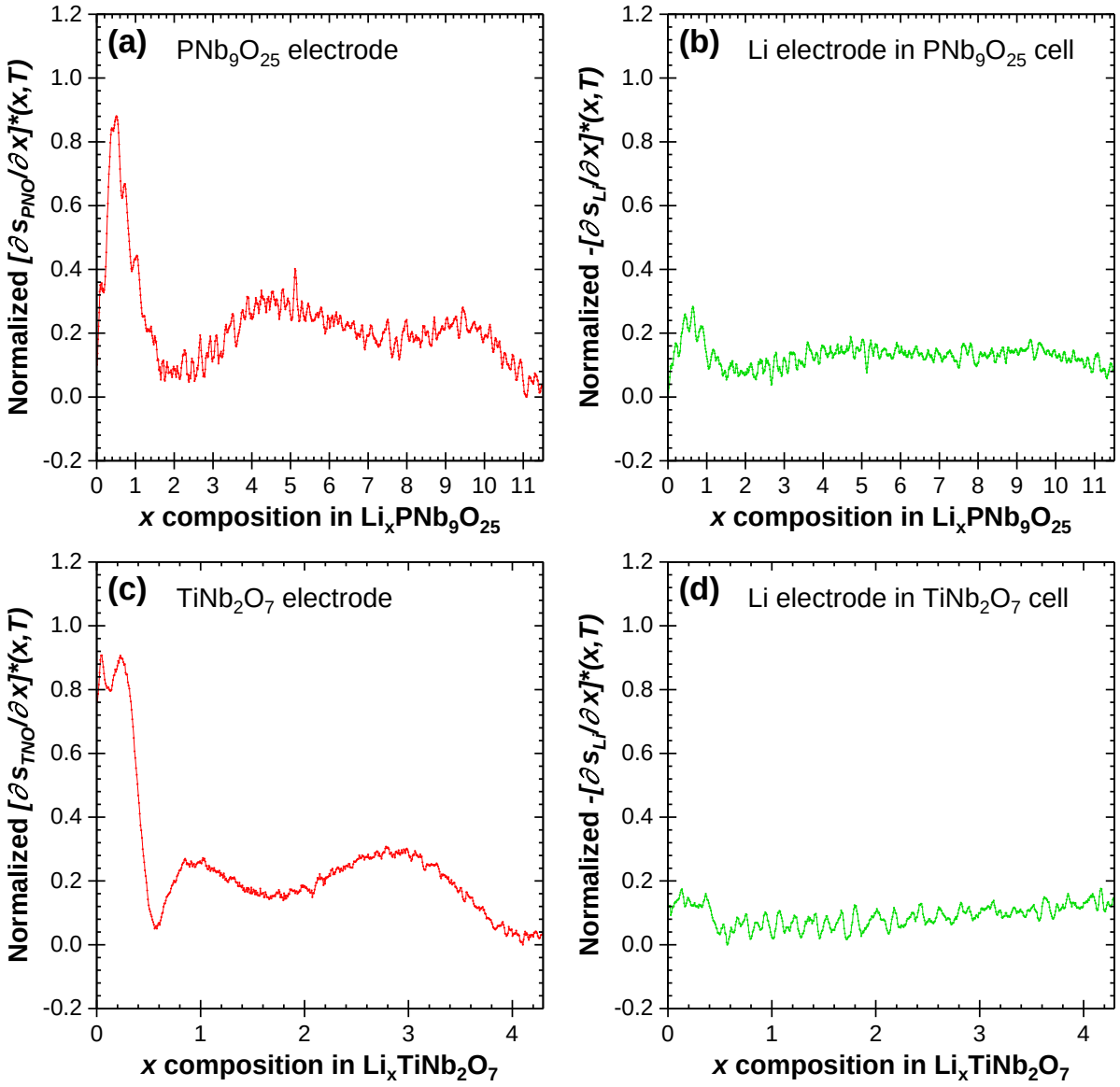

Figure 8: Normalized partial entropy changes (a) $[\partial s_{PNO}/\partial x]^*(x,T)$ at the PNb_9O_{25} working electrode or (c) $[\partial s_{TNO}/\partial x]^*(x,T)$ at the $TiNb_2O_7$ working electrode determined by microcalorimetry ETIS measurements. (b, d) Normalized partial entropy changes $-[\partial s_{Li}/\partial x]^*(x,T)$ at the corresponding metallic lithium counter electrode.

$TiNb_2O_7$ working electrodes and at the corresponding metallic lithium counter electrodes according to Equations (39) and (42). Here also, the partial entropy changes were normalized, i.e., at electrode "j" (= PNO, TNO, or Li) according to,

$$\left[\frac{\partial s_j}{\partial x}\right]^*(x,T) = \frac{(1/e)[\partial s_j/\partial x](x,T) - (1/e)[\partial s_j/\partial x]_{min}(x,T)}{[\partial U_{OCV}/\partial T]_{max}(x,T) - [\partial U_{OCV}/\partial T]_{min}(x,T)} \tag{46}$$

where $[\partial s_j/\partial x]_{min}(x,T)$ is the minimum value of the partial entropy change $[\partial s_j/\partial x](x,T)$ over the entire window of lithium composition. For comparison, Figure 8 plots the normalized partial entropy changes $[\partial s_j/\partial x]^*(x,T)$ at the PNb_9O_{25} or $TiNb_2O_7$ working electrodes and at the corresponding metallic lithium counter electrodes. Here, the normalized partial entropy changes $[\partial s_{PNO}/\partial x]^*(x,T)$ or $[\partial s_{TNO}/\partial x]^*(x,T)$ at the working electrodes essentially replicated qualitatively the features of the normalized entropic potential $[\partial U_{OCV}/\partial T]^*(x,T)$ for the full cell. By contrast, the normalized partial entropy changes $-[\partial s_{Li}/\partial x]^*(x,T)$ at the counter electrodes stayed relatively constant near 0 with varying state of charge. Such behavior was consistent with our previous theoretical derivation [7]. Specifically, the partial entropy change $-[\partial s_{Li}/\partial x](x,T)$ at the metallic lithium counter electrode should be equal to the standard entropy per unit of metallic lithium $-s^\circ_{Li}(T)$ and thus independent of x. Therefore, $-[\partial s_{Li}/\partial x]^*(x,T)$ should theoretically be equal to 0, as confirmed by Figure (8). This suggests that continuous lithium stripping and plating were the dominant processes occurring at the counter electrodes. Overall, these results demonstrate the capability of the novel microcalorimetry ETIS method to extract the partial entropy changes at each electrode, which has not been achieved by any other existing method.

6 Conclusion

This paper presented a novel and fast microcalorimetry ETIS measurement method using an *operando* isothermal calorimeter to determine the open-circuit voltage U_{OCV}, the entropic potential $\partial U_{OCV}/\partial T$, and the partial entropy changes at each electrode as functions of the state of charge of a battery cell, all within only a few hours. The apparatus was designed for bare electrodes (i.e., without casing) with material mass loadings on the order of mil-

ligrams and measured heat generation rates on the order of microwatts. The method consists of imposing a sinusoidal current and measuring the potential response as well as the heat generation rates at each electrode separately. The open-circuit voltage U_{OCV} of the cell was acquired by time-averaging the measured potential response. Furthermore, FFT analysis of the measured total heat generation rate was used to retrieve the entropic potential $\partial U_{OCV}/\partial T$ of the entire cell without having to measure the cell potential at several different temperatures. The procedure was first validated numerically and then demonstrated experimentally with battery cells consisting of PNb_9O_{25} or $TiNb_2O_7$ working electrodes and metallic lithium counter electrodes. The open-circuit voltage and the normalized entropic potential retrieved from the novel microcalorimetry ETIS measurements agreed well with those previously determined by potentiometric entropy measurements based on GITT at three different temperatures [27, 28]. Finally, the partial entropy changes at each electrode were calculated from the individually measured heat generation rates. Compared to other state-of-the-art methods, this is the first method capable of retrieving the entropy evolution of LIB materials at each electrode.

7 Acknowledgment

This work was supported by the Center for Synthetic Control Across Length-scales for Advancing Rechargeables (SCALAR), an Energy Frontier Research Center funded by the U.S. Department of Energy, Office of Science, Basic Energy Sciences, under Award No. DE-SC0019381.

References

[1] A. K. Shukla, T. P. Kumar, Materials for next-generation lithium batteries, Current Science 94 (3) (2008) 314–331.

[2] J. Cao, A. Emadi, A new battery/ultracapacitor hybrid energy storage system for electric, hybrid, and plug-in hybrid electric vehicles, IEEE Transactions on Power Electronics 27 (1) (2011) 122–132. doi:10.1109/TPEL.2011.2151206.

[3] H. Kim, G. Jeong, Y.-U. Kim, J.-H. Kim, C.-M. Park, H.-J. Sohn, Metallic anodes for next generation secondary batteries, Chemical Society Reviews 42 (23) (2013) 9011–9034. doi:10.1039/C3CS60177C.

[4] L. Lu, X. Han, J. Li, J. Hua, M. Ouyang, A review on the key issues for lithium-ion battery management in electric vehicles, Journal of Power Sources 226 (2013) 272–288. doi:10.1016/j.jpowsour.2012.10.060.

[5] J. Zhang, L. Zhang, F. Sun, Z. Wang, An overview on thermal safety issues of lithium-ion batteries for electric vehicle application, IEEE Access 6 (2018) 23848–23863. doi:10.1109/ACCESS.2018.2824838.

[6] M. Walter, M. V. Kovalenko, K. V. Kravchyk, Challenges and benefits of post-lithium-ion batteries, New Journal of Chemistry 44 (5) (2020) 1677–1683. doi:10.1039/C9NJ05682C.

[7] S. W. Baek, M. Saber, A. Van der Ven, L. Pilon, Thermodynamic analysis and interpretative guide to entropic potential measurements of lithium-ion battery electrodes, The Journal of Physical Chemistry C 126 (14) (2022) 6096–6110. doi:10.1021/acs.jpcc.1c10414.

[8] P. J. Osswald, M. Rosario, J. Garche, A. Jossen, H. E. Hoster, Fast and accurate measurement of entropy profiles of commercial lithium-ion cells, Electrochimica Acta 177 (2015) 270–276. doi:10.1016/j.electacta.2015.01.191.

[9] N. Damay, C. Forgez, M.-P. Bichat, G. Friedrich, A method for the fast estimation of a battery entropy-variation high-resolution curve – application on a commercial $LiFePO_4$/graphite cell, Journal of Power Sources 332 (2016) 149–153. doi:10.1016/j.jpowsour.2016.09.083.

[10] K. A. Murashko, A. V. Mityakov, V. Y. Mityakov, S. Z. Sapozhnikov, J. Jokiniemi, J. Pyrhonen, Determination of the entropy change profile of a cylindrical lithium-ion battery by heat flux measurements, Journal of Power Sources 330 (2016) 61–69. doi:10.1016/j.jpowsour.2016.08.130.

[11] E. M. Perassi, E. P. M. Leiva, A theoretical model to determine intercalation entropy and enthalpy: application to lithium/graphite, Electrochemistry Communications 65 (2016) 48–52. doi:10.1016/j.elecom.2016.02.003.

[12] M. Lenz, T. Hoehl, L. Zanger, S. Pischinger, Approach to determine the entropy coefficient of a battery by numerical optimization, Journal of Power Sources 480 (2020) 228841. doi:10.1016/j.jpowsour.2020.228841.

[13] A. Abbasalinejad, M. M. Besli, J. W. Hammond, S. H. Chung, J. Christensen, S. U. Kim, Evaluation of the entropy of reaction using modified frequency-domain method and a physics-based thermoelectrochemical model of a lithium-ion battery, Journal of Power Sources 508 (2021) 230283. doi:10.1016/j.jpowsour.2021.230283.

[14] A. M. Ahmad, G. Thenaisie, S.-G. Lee, A calorimetric approach to fast entropy-variations extraction for lithium-ion batteries using optimized galvanostatic intermittent titration technique, Journal of Power Sources Advances 16 (2022) 100097. doi:10.1016/j.powera.2022.100097.

[15] Z. Lin, D. Wu, C. Du, Z. Ren, An improved potentiometric method for the measurement of entropy coefficient of lithium-ion battery based on positive adjustment, Energy Reports 8 (2022) 54–63. doi:10.1016/j.egyr.2022.10.109.

[16] G. K. Mertin, D. Wycisk, M. Oldenburger, G. Stoye, A. Fill, K. P. Birke, A. D. Wieck, Dynamic measurement of the entropy coefficient for battery cells, Journal of Energy Storage 51 (2022) 104361. doi:10.1016/j.est.2022.104361.

[17] J. P. Schmidt, A. Weber, E. Ivers-Tiffee, A novel and precise measuring method for the entropy of lithium-ion cells: ΔS via electrothermal impedance spectroscopy, Electrochimica Acta 137 (2014) 311–319. doi:10.1016/j.electacta.2014.05.153.

[18] Y. Hu, S.-Y. Choe, Simultaneous and continuous characterization of reversible and irreversible heat of lithium-ion battery using wavelet transform technique, Electrochimica Acta 375 (2021) 137973. doi:10.1016/j.electacta.2021.137973.

[19] Y. Hu, S.-Y. Choe, T. R. Garrick, Measurement of heat generation rate and heat sources of pouch type Li-ion cells, Applied Thermal Engineering 189 (2021) 116709. doi:10.1016/j.applthermaleng.2021.116709.

[20] M. B. Preefer, M. Saber, Q. Wei, N. H. Bashian, J. D. Bocarsly, W. Zhang, G. Lee, J. Milam-Guerrero, E. S. Howard, R. C. Vincent, B. C. Melot, A. Van der Ven, R. Seshadri, B. S. Dunn, Multielectron redox and insulator-to-metal transition upon lithium insertion in the fast-charging, Wadsley-Roth phase PNb_9O_{25}, Chemistry of Materials 32 (11) (2020) 4553–4563. doi:10.1021/acs.chemmater.0c00560.

[21] R. C. Vincent, Y. Luo, J. L. Andrews, A. Zohar, Y. Zhou, Q. Yan, E. M. Mozur, M. B. Preefer, J. N. Weker, A. K. Cheetham, J. Luo, L. Pilon, B. C. Melot, B. Dunn, R. Seshadri, High-rate lithium cycling and structure evolution in Mo_4O_{11}, Chemistry of Materials 34 (9) (2022) 4122–4133. doi:10.1021/acs.chemmater.2c00420.

[22] K. E. Wyckoff, J. L. Kaufman, S. W. Baek, C. Dolle, J. J. Zak, J. Bienz, L. Kautzsch, R. C. Vincent, A. Zohar, K. A. See, Y. M. Eggeler, L. Pilon, A. Van der Ven, R. Seshadri, Metal-metal bonding as an electrode design principle in the low-strain cluster compound $LiScMo_3O_8$, Journal of the American Chemical Society 144 (13) (2022) 5841–5854. doi:10.1021/jacs.1c12070.

[23] A. Van der Ven, J. Bhattacharya, A. A. Belak, Understanding Li diffusion in Li-intercalation compounds, Accounts of Chemical Research 46 (5) (2013) 1216–1225. doi:10.1021/ar200329r.

[24] M. J. Moran, H. N. Shapiro, D. D. Boettner, M. B. Bailey, Fundamentals of Engineering Thermodynamics, John Wiley & Sons, New York, NY, 2018.

[25] A. Van der Ven, M. Wagemaker, Effect of surface energies and nano-particle size distribution on open circuit voltage of Li-electrodes, Electrochemistry Communications 11 (4) (2009) 881–884. doi:10.1016/j.elecom.2009.02.015.

[26] M. W. Chase, NIST-JANAF Thermochemical Tables, American Chemical Society, Washington DC, 1998.

[27] S. W. Baek, K. E. Wyckoff, D. M. Butts, J. Bienz, A. Likitchatchawankun, M. B. Preefer, M. Frajnkovič, B. S. Dunn, R. Seshadri, L. Pilon, *Operando* calorimetry informs the origin of rapid rate performance in microwave-prepared $TiNb_2O_7$ electrodes, Journal of Power Sources 490 (2021) 229537. doi:10.1016/j.jpowsour.2021.229537.

[28] S. W. Baek, M. B. Preefer, M. Saber, K. Zhai, M. Frajnkovič, Y. Zhou, B. S. Dunn, A. Van der Ven, R. Seshadri, L. Pilon, Potentiometric entropy and *operando* calorimetric measurements reveal fast charging mechanisms in PNb_9O_{25}, Journal of Power Sources 520 (2022) 230776. doi:10.1016/j.jpowsour.2021.230776.

[29] Y. Zhou, E. Le Calvez, S. W. Baek, M. Frajnkovič, C. Douard, E. Gautron, O. Crosnier, T. Brousse, L. Pilon, Effect of particle size on thermodynamics and lithium ion transport in electrodes made of $Ti_2Nb_2O_9$ microparticles or nanoparticles, Energy Storage Materials 52 (2022) 371–385. doi:10.1016/j.ensm.2022.08.010.

[30] G. Assat, S. L. Glazier, C. Delacourt, J.-M. Tarascon, Probing the thermal effects of voltage hysteresis in anionic redox-based lithium-rich cathodes using isothermal calorimetry, Nature Energy 4 (8) (2019) 647–656. doi:10.1038/s41560-019-0410-6.

[31] X. Feng, M. Fang, X. He, M. Ouyang, L. Lu, H. Wang, M. Zhang, Thermal runaway features of large format prismatic lithium ion battery using extended volume accelerating rate calorimetry, Journal of Power Sources 255 (2014) 294–301. doi:10.1016/j.jpowsour.2014.01.005.

[32] Y. Wang, K. Zaghib, A. Guerfi, F. F. C. Bazito, R. M. Torresi, J. R. Dahn, Accelerating rate calorimetry studies of the reactions between ionic liquids and charged lithium ion battery electrode materials, Electrochimica Acta 52 (22) (2007) 6346–6352. doi:10.1016/j.electacta.2007.04.067.

[33] A. Du Pasquier, F. Disma, T. Bowmer, A. S. Gozdz, G. Amatucci, J.-M. Tarascon, Differential scanning calorimetry study of the reactivity of carbon anodes in plastic Li-ion batteries, Journal of The Electrochemical Society 145 (2) (1998) 472–477. doi:10.1149/1.1838287.

[34] H. Giel, D. Henriques, G. Bourne, T. Markus, Investigation of the heat generation of a commercial 2032 ($LiCoO_2$) coin cell with a novel differential scanning battery calorimeter, Journal of Power Sources 390 (2018) 116–126. doi:10.1016/j.jpowsour.2018.04.017.

[35] Y. Saito, K. Kanari, K. Takano, Thermal studies of a lithium-ion battery, Journal of Power Sources 68 (2) (1997) 451–454. doi:10.1016/S0378-7753(96)02583-9.

[36] O. Munteshari, J. Lau, A. Krishnan, B. Dunn, L. Pilon, Isothermal calorimeter for measurements of time-dependent heat generation rate in individual supercapacitor electrodes, Journal of Power Sources 374 (2018) 257–268. doi:10.1016/j.jpowsour.2017.11.012.

[37] O. Munteshari, J. Lau, D. S. Ashby, B. Dunn, L. Pilon, Effects of constituent materials on heat generation in individual EDLC electrodes, Journal of The Electrochemical Society 165 (7) (2018) A1547–A1557. doi:10.1149/2.0771807jes.

[38] A. Likitchatchawankun, A. Kundu, O. Munteshari, T. S. Fisher, L. Pilon, Heat generation in all-solid-state supercapacitors with graphene electrodes and gel electrolytes, Electrochimica Acta 303 (2019) 341–353. doi:10.1016/j.electacta.2019.02.031.

[39] A. Likitchatchawankun, G. Whang, J. Lau, O. Munteshari, B. Dunn, L. Pilon, Effect of temperature on irreversible and reversible heat generation rates in ionic liquid-based electric double layer capacitors, Electrochimica Acta 338 (2020) 135802. doi:10.1016/j.electacta.2020.135802.

[40] O. Munteshari, A. Borenstein, R. H. DeBlock, J. Lau, G. Whang, Y. Zhou, A. Likitchatchawankun, R. B. Kaner, B. Dunn, L. Pilon, *In operando* calorimetric measurements for activated carbon electrodes in ionic liquid electrolytes under large potential windows, ChemSusChem 13 (5) (2020) 1013–1026. doi:10.1002/cssc.201903011.

[41] A. Likitchatchawankun, R. H. DeBlock, G. Whang, O. Munteshari, M. Frajnkovič, B. S. Dunn, L. Pilon, Heat generation in electric double layer capacitors with neat and diluted ionic liquid electrolytes under large potential window between 5 and 80 °C, Journal of Power Sources 488 (2021) 229368. doi:10.26434/chemrxiv.13168349.

[42] O. Munteshari, J. Lau, A. Likitchatchawankun, B.-A. Mei, C. S. Choi, D. Butts, B. S. Dunn, L. Pilon, Thermal signature of ion intercalation and surface redox reactions mechanisms in model pseudocapacitive electrodes, Electrochimica Acta 307 (2019) 512–524. doi:10.1016/j.electacta.2019.03.185.

[43] M. Frajnkovič, A. Likitchatchawankun, C. Douard, Y. Zhou, S. W. Baek, I. Catton, O. Crosnier, T. Brousse, L. Pilon, Calorimetry can detect the early onset of hydrolysis in hybrid supercapacitors with aqueous electrolytes, Journal of Power Sources 548 (2022) 232069. doi:10.1016/j.jpowsour.2022.232069.

[44] M. Frigo, S. G. Johnson, FFTW: an adaptive software architecture for the FFT, in: Proceedings of the 1998 IEEE International Conference on Acoustics, Speech and

Signal Processing, ICASSP '98 (Cat. No.98CH36181), Vol. 3, 1998, pp. 1381–1384. doi:10.1109/ICASSP.1998.681704.

[45] L. H. Hess, A. Bothe, A. Balducci, Design and use of a novel in situ simultaneous thermal analysis cell for an accurate "real time" monitoring of the heat and weight changes occurring in electrochemical capacitors, Energy Technology 9 (9) (2021) 2100329. doi:10.1002/ente.202100329.

[46] A. Bothe, A. Balducci, Thermal analysis of electrical double layer capacitors: Present status and remaining challenges, Journal of Power Sources 548 (2022) 232090. doi:10.1016/j.jpowsour.2022.232090.

[47] A. Bothe, S. E. M. Pourhosseini, P. Ratajczak, F. Beguin, A. Balducci, Analysis of thermal and electrochemical properties of electrical double-layer capacitors by using an in-situ simultaneous thermal analysis cell, Electrochimica Acta 444 (2023) 141974. doi:10.1016/j.electacta.2023.141974.

[48] J. P. Schmidt, D. Manka, D. Klotz, E. Ivers-Tiffee, Investigation of the thermal properties of a Li-ion pouch-cell by electrothermal impedance spectroscopy, Journal of Power Sources 196 (19) (2011) 8140–8146. doi:10.1016/j.jpowsour.2011.05.047.

[49] Z. Li, B.-A. Mei, Complex thermal analysis of supercapacitor by thermal impedance spectroscopy, Thermochimica Acta 710 (2022) 179175. doi:10.1016/j.tca.2022.179175.

[50] B.-A. Mei, O. Munteshari, J. Lau, B. Dunn, L. Pilon, Physical interpretations of Nyquist plots for EDLC electrodes and devices, The Journal of Physical Chemistry C 122 (1) (2018) 194–206. doi:10.1021/acs.jpcc.7b10582.

[51] B.-A. Mei, J. Lau, T. Lin, S. H. Tolbert, B. S. Dunn, L. Pilon, Physical interpretations of electrochemical impedance spectroscopy of redox active electrodes for electrical energy storage, The Journal of Physical Chemistry C 122 (43) (2018) 24499–24511. doi:10.1021/acs.jpcc.8b05241.

[52] J. Newman, K. E. Thomas, H. Hafezi, D. R. Wheeler, Modeling of lithium-ion batteries, Journal of Power Sources 119 (2003) 838–843. doi:10.1016/S0378-7753(03)00282-9.

[53] G. Liu, M. Ouyang, L. Lu, J. Li, X. Han, Analysis of the heat generation of lithium-ion battery during charging and discharging considering different influencing factors, Journal of Thermal Analysis and Calorimetry 116 (2) (2014) 1001–1010. doi:10.1007/s10973-013-3599-9.

[54] K. Smith, C.-Y. Wang, Power and thermal characterization of a lithium-ion battery pack for hybrid-electric vehicles, Journal of Power Sources 160 (1) (2006) 662–673. doi:10.1016/j.jpowsour.2006.01.038.

[55] M. Saber, M. B. Preefer, S. K. Kolli, W. Zhang, G. Laurita, B. Dunn, R. Seshadri, A. Van der Ven, Role of electronic structure in Li ordering and chemical strain in the fast charging Wadsley-Roth phase PNb_9O_{25}, Chemistry of Materials 33 (19) (2021) 7755–7766. doi:10.1021/acs.chemmater.1c02059.

[56] K. J. Griffith, I. D. Seymour, M. A. Hope, M. M. Butala, L. K. Lamontagne, M. B. Preefer, C. P. Kocer, G. Henkelman, A. J. Morris, M. J. Cliffe, S. E. Dutton, C. P. Grey, Ionic and electronic conduction in $TiNb_2O_7$, Journal of the American Chemical Society 141 (42) (2019) 16706–16725. doi:10.1021/jacs.9b06669.

[57] P. Zhai, L. Liu, X. Gu, T. Wang, Y. Gong, Interface engineering for lithium metal anodes in liquid electrolyte, Advanced Energy Materials 10 (34) (2020) 2001257. doi:10.1002/aenm.202001257.

[58] Y. Han, B. Liu, Z. Xiao, W. Zhang, X. Wang, G. Pan, Y. Xia, X. Xia, J. Tu, Interface issues of lithium metal anode for high-energy batteries: Challenges, strategies, and perspectives, InfoMat 3 (2) (2021) 155–174. doi:10.1002/inf2.12166.